Establishing Quantitative Measures of Quality of Functional Near Infrared Spectroscopy Data

by

Dhanalakshmi Gopal Dhamodaran

A thesis submitted to the Department of Engineering Technology,

College of Technology

in partial fulfillment of the requirements for the degree of

Master of Science
in Engineering Technology

Chair of Committee: Dr. Luca Pollonini, Assistant Professor, University of Houston

Committee Member: Dr. George Zouridakis, Professor, University of Houston

Committee Member: Dr. Fatima A. Merchant, Associate Professor, University of Houston

University of Houston
May 2020

ABSTRACT

Functional Near-Infrared Spectroscopy (fNIRS) is an optical neuroimaging technique that can be used to examine and quantify tissue hemodynamics on the brain. fNIRS signals are contaminated by measurement noises and physiology-based systemic noises, such as a periodic pulsation of optical signals associated with the cardiac activity. Several approaches exist to filter out all sorts of noises and to remove channels with a low signal-to-noise ratio (SNR) that are deemed unreliable to estimate cortical hemodynamics. However, amongst the systemic noises which are undesirable for cerebral hemodynamics, strong cardiac pulsations usually indicate a good contact between the optical probe and the scalp.

This thesis aims at evaluating the performance of physiology-based measures of quality of fNIRS data, namely 1) the Scalp Contact Index (SCI) and 2) the Peak Power (PP) of the spectrum, and understand how would they vary as a function of a range of pair of wavelengths, and for experiments conducted with different experimental setups such as 1) the source-detector distance, 2) the integration time of photodetectors and 3) the anatomical location on the head where signals are collected.

So, while keeping other parameters constant, we are going to vary only one parameter at a time and collect the data and compute the SCI and PP for that data to compare its quality.

TABLE OF CONTENTS

1. INTRODUCTION

Functional near-infrared spectroscopy (fNIRS) is widely used as an optical brain imaging technology as near-infrared light is non-invasive, non-ionizing and the experimentation is very adaptable, easy, portable, and relatively inexpensive.

One of the most invaluable neuroimaging tools is functional magnetic resonance imaging (fMRI), which offers excellent spatial resolution for measuring local changes in cerebral oxygenation and blood flow, evoked during functional tasks [1]. Though it is excellent to study the primary functional regions of the brain, the process of the study limits the mobility as the patients must remain still throughout the experiment inside the MRI magnet [2].

The growth of fNIRS research began in 1977 when it was first reported that biological tissues can transmit near-infrared light through them over significant distances [3]. Since then fNIRS has been a very promising area of research mainly in three domains: object processing, processing of biologically and socially relevant information, and language development [4]. As there is a correlation between fNIRS and fMRI activations during motor tasks from concurrent multimodal recordings, fNIRS became prominent as an alternative neuroimaging tool with increased ambulation and high adaptability [5]. Neuroimaging researches involving infants, old adults, and studies related to the behavior of the whole body such as walking, exercise are some of the significant contributions. Still, fNIRS is also bound to some limitations to its applications such as lower spatial resolution and limited recording of the brain depth compared to fMRI [6]. Thus, recent multimodal approaches are being developed combining the advantages of fNIRS and fMRI which helps in researches involving complicated concepts that cannot be solved with just of either approach. NIRS is also called near-infrared imaging (NIRI), diffuse optical topography or tomography (DOT), diffuse optical imaging (DOI), while the physiological concepts and fundamental ideas are the same [7].

1.1. Measuring the cortical activity using the modified Beer-Lambert law

Based on the typical backscattering nature of human tissues, tissue hemodynamics can be quantified as an optical absorption measurement by using the reflective optical scheme. Since neuronal activation requires increased oxygen carried by blood, cortical hemodynamics is a representation of functional brain activity.

Beer Lambert's law states that the quantity of light absorbed by a substance dissolved in a fully transmitting solvent is directly proportional to the concentration of the chromophore and the path length of the light.

$$A = \log\left(\frac{I_{inc}}{I_{det}}\right) = \alpha c d$$

In this equation, Inc is the incident light intensity and Idet is the detected light intensity. c is the concentration of the substance. d is the distance from where light enters the tissue to where it leaves the tissue and α is the absorption coefficient of the chromophore. The absorption coefficient describes the intensity attenuation of the light passing through a material.

The brain activity is measured by recording changes in how much light the brain absorbs by using the modified Beer-Lambert law [8]. The modified Beer-Lambert law (MBLL) forms the basis of any Continuous-wave near-infrared tissue spectroscopy (cwNIRS), named as they continuously emit at a constant amplitude. The tissue is a highly scattering medium and d does not reflect the true path length. Scattering significantly prolongs the path length of light. To account for that, the modified Beer-Lambert law is used:

$$I(\lambda) = I_o(\lambda)\, e^{-\mu a(\lambda)\, d\, DPF(\lambda) + G(\lambda)}$$

where d is the source-detector separation, DPF(λ) differential path length factor, is a multiplier factor that accounts for the increased curved path and G(λ) is a constant anisotropy factor representing scattering loss and solely depends on the geometry (not on absorption). The fact that

the head is inhomogeneous is not a problem, because the inhomogeneity remains constant and is mostly covered by the constant G.

The modified Beer-Lambert law (MBLL) [9] states that the changes in measured light intensities are converted into changes in oxy- and deoxyhemoglobin in the underlying brain. Brain tissues have three significant chromophores: water, oxy-hemoglobin (oxy-Hb), and deoxyhemoglobin (deoxy-Hb). In functional brain imaging applications, the main interest is to monitor oxy-Hb and deoxy-Hb concentration changes. Within the 700-900nm range, also called as 'optical window', the tissue is relatively transparent because all significant chromophore absorption factors are low. The dominant chromophores in the optical window are oxy-Hb and deoxy-Hb, and their concentration changes can be calculated

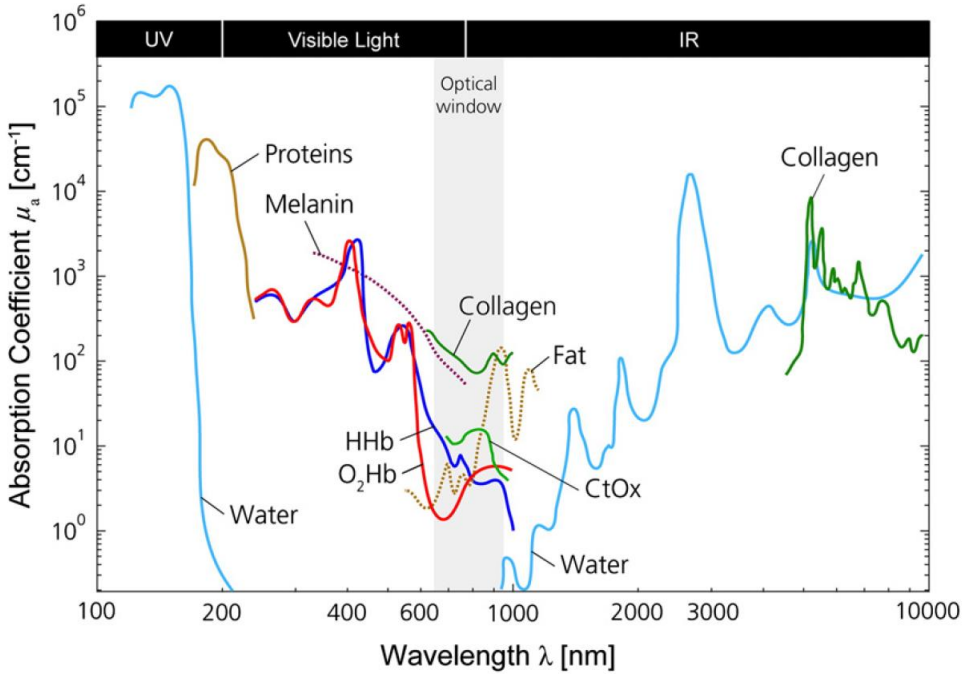

Figure 1: The optical window showing the absorption factors of the three main chromophores concerning wavelength. This Figure is taken from [9]

Within the optical window, there is an isosbestic point where the absorption spectra of oxy-Hb and deoxy-Hb cross. Measurements by choosing two wavelengths, one below and one above this

isosbestic point, could reveal the individual effects of oxy-Hb and deoxy-Hb [9]. In the MBLL, d is known, DPF can be estimated with simulations of light propagation in tissues. Assuming that the change in scattering is small compared to the change in absorption, G can be assumed to be time-invariant. Hence G cancels out while measuring concentration changes.

To calculate the changes in the attenuation, we need to compare two measurements of the detected intensities at two different states of the tissue which is proportional to the absorption changes [10]. Calling L= d. DPF, the mean pathlength of detected photons:

MBLL : $A = l_n \frac{I_{inc}}{I_{det}} = L\mu_a + G$

Differential MBLL : $\Delta A = l_n \frac{I_{det,1}}{I_{det,2}} = L\Delta\mu_a$

For two different wavelengths $\lambda_1$and λ_2, considering the only oxy- and deoxy-hemoglobin the only two absorbers, the total concentration change is given as :

$$\Delta\mu_a = \alpha_{HbO_2}\Delta c_{HbO_2} + \alpha_{Hb}\Delta c_{Hb}$$

where α_{HbO_2} and α_{Hb} denote the molar absorption coefficients of oxyhemoglobin (HbO) and deoxyhemoglobin (HbR) respectively.

$$\Delta c_{HbO_2} = \frac{\alpha_{Hb}^{\lambda_1}\frac{\Delta A^{\lambda_2}}{L^{\lambda_2}} - \alpha_{Hb}^{\lambda_2}\frac{\Delta A^{\lambda_1}}{L^{\lambda_1}}}{\alpha_{Hb}^{\lambda_1}\alpha_{HbO_2}^{\lambda_2} - \alpha_{Hb}^{\lambda_2}\alpha_{HbO_2}^{\lambda_1}}$$

$$\Delta c_{Hb} = \frac{\alpha_{HbO_2}^{\lambda_1}\frac{\Delta A^{\lambda_2}}{L^{\lambda_2}} - \alpha_{HbO_2}^{\lambda_2}\frac{\Delta A^{\lambda_1}}{L^{\lambda_1}}}{\alpha_{HbO_2}^{\lambda_1}\alpha_{Hb}^{\lambda_2} - \alpha_{HbO_2}^{\lambda_2}\alpha_{Hb}^{\lambda_1}}$$

These equations show that Δc_{HbO_2} and Δc_{Hb} which are the concentration changes of oxyhemoglobin (HbO) and deoxyhemoglobin (HbR) respectively, within the region brain activation are associated with local optical absorption changes in the near-infrared spectral range (650-1000 nm).

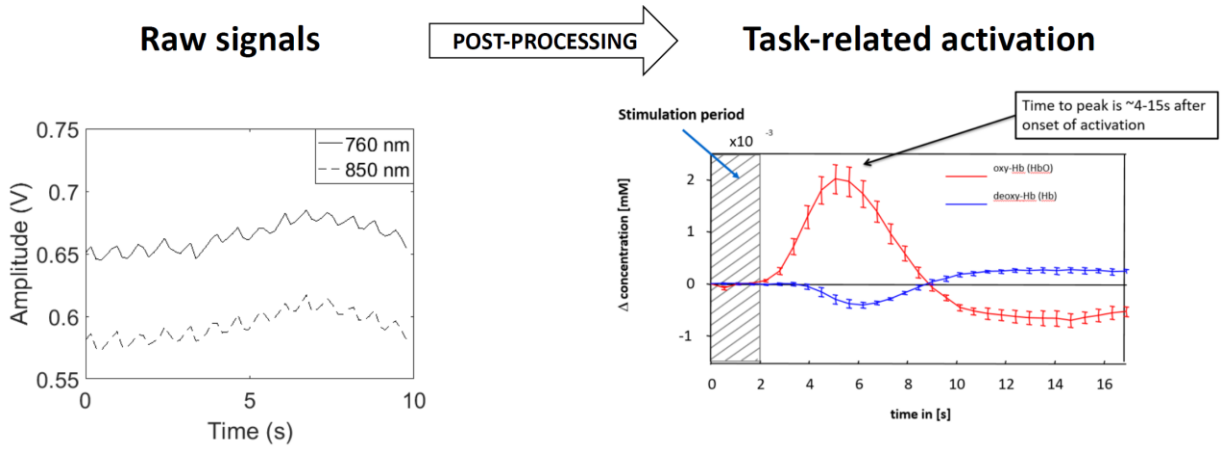

Figure 2: The raw fNIRS signals converted into the concentration changes after the onset of activation in the brain. The image is taken from Dr. Pollonini's course ELET 6397 Optical Brain Imaging lecture slides.

Hence the brain function can be studied at various parts of the brain by placing the optodes with a spacing of few centimeters and emitting the light from the source that can travel deep into the brain to several centimeters of 5 to 8 mm of the brain cortex and detected back [11].

1.2. fNIRS Data Analysis

The fNIRS data analysis mostly consists of two phases of preprocessing and post-processing. During preprocessing the data undergoes data preparation, noise filtering, and motion artifacts correction. Post-processing may include block average, model-based regression, and statistical calculations. Many recent developments have been made in the field of fNIRS applications and procedures from the simple modified Beer-Lambert law to fNIRS analysis using NIRx, NIRS Analysis in Homer2, the MATLAB NIRS Toolbox, a MATLAB-based software package for statistical analysis called NIRS SPM, a set of MATLAB functions called NFRI Toolbox to perform probabilistic registrations, and more advancements have been made to the fNIRS data analysis [12]. Due to these developments, fNIRS is widely being used in neuroscience research and several manufacturers provide commercial instrumentation.

1.3. Signal contamination and de-noising techniques

However, fNIRS signals are known to contain various noises, such as physiological noises (i.e., heartbeat, respiration, vasomotion, and Mayer waves), extra-cortical physiological noises from the superficial layer (i.e. scalp), and motion artifacts. This type of cardiac noise is mainly located near large blood vessels, and respiratory noise correspondingly on the edges of the brain, and in the larger veins and ventricles, their frequency bands were identified as cardiac (0.8 to 1.5 Hz), respiration (0.1 to 0.6 Hz) [13][14]. Vasomotion and Mayer waves are the two other low-frequency hemodynamic oscillations in a nearby spectral region (0.1–0.4 Hz). Meyer waves are the spontaneous hemodynamic oscillations in arterial blood pressure. Vasomotion is created as a flow motion when the cross-section of blood vessels oscillate due to the oscillations in the tone of blood vessels [15].

Motion artifacts can have different shapes, frequency content, and timing. Motion artifacts can be generally classified into three categories, spikes, baseline shifts, and low-frequency variations (Figure 3). Therefore, it is likely that the efficacy of each motion artifact correction technique will vary with the type of motion artifact and that the best technique to apply is data dependent. Furthermore, motion artifacts are not only due to the movement of the head but also due to the movement of the eyebrows or the jaw [16].

These noises lead to errors in the collected data and should be removed to properly investigate brain functions [18]. A lot of filtering methods are developed to remove these noise frequencies from the data, the high pass filters to remove the low-frequency systemic noises and the low-pass filters to remove the cardiac pulsations and other high-frequency instrumental noise [6]. Many de-noising approaches have been developed recently using digital filters, optimized experimental paradigms, or pre-processing methods for the fNIRS data which greatly improve the accuracy and sensitivity of fNIRS measurements corrected, but only a few approaches focus on the automatic elimination of noisy channels.

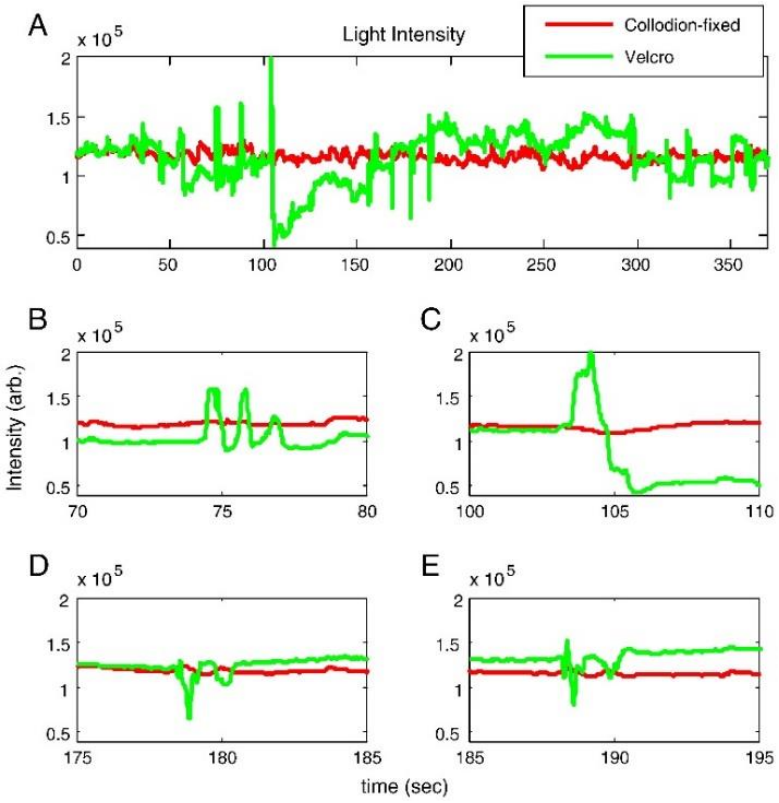

Figure 1: Image taken from [17] : Raw NIRS signal from a pair of NIRS channel during a 6-minute run (A), examples of individual motion artifacts (B, C, D and E) as recorded from collodion-fixed fiber probe and Velcro probe at 690 nm. (A) shows the entire signal and we can see the movement of the subject produces noticeably smaller amplitude artifacts in the signal recorded using the collodion-fixed probe. An example of a motion-induced shift in baseline signal is shown in (C). While the shift is maintained even after the movement at the Velcro probe side, the signal level is recovered at the collodion-fixed fiber probe side.

Experimental errors can be eliminated by placing the source and detector channels positioned properly in the scalp to get the maximum optical signals needed for the study. Though a good optode-scalp coupling could be achieved by learning through the experience of properly placing the headgear, it could also be effectively monitored if there is a quantitative measure to assess the optode-scalp coupling as a signal to noise ratio which could be checked before the experiment for a good data collection. Such a numerical value used to measure the quality of a channel is called the scalp coupling index (SCI). And another numerical value to detect the error occurred in the channel due to a motion artifact is called the peak spectral power(PP) [20] [19].

1.4. Background

Using a single pair of optodes restricts the area of imaging to the cortical region between the optodes. So, using a greater number of source and detector optodes around the head can provide a hemodynamic image of the entire cerebral cortex. One of the main challenges encountered by fNIRS researchers is collecting optical signals with a signal-to-noise ratio (SNR) from the entire set of channels that is good enough to carry out a reliable estimation of cortical hemodynamics.

While setting up an experiment to study the entire cortex, headgear with several optodes will be fitted on the scalp of the subject. In that situation, few or more optodes might collect poor signals due to the obstruction of the hair. Hence it is important to distinctively localize the optodes which do not make good contact with the scalp so that they can be adjusted to fit properly. These implementations have been used as a method in the software tool called PHOEBE (Placing Headgear Optodes Efficiently Before Experimentation) developed by Dr.Pollonini and his colleagues [19]. PHOEBE is a MATLAB GUI application that displays optode coupling strength of all the optodes around the scalp of a subject in real-time. It was done by measuring the signal to noise ratio between each channel. It is aimed to reduce the time needed in setting up the experiment and increased the quality of signal collection by enhancing the signal to noise ratio of all the channels. But, the SCI and PP was able to be determined for only one wavelength pair 760 nm and 850 nm in the NIRx NIRSScout and 40 optodes as optical channels were used with optode inter-distance between 30mm and 45mm.

The goal of the thesis is to study more about the performance of SCI and PP is to understand how these measures vary when a range of wavelengths pairs are used for the data collected from different experiment setups, from different anatomical locations of the head, and to set a common ground of standardization for the quality of the fNIRS data.

2. MATERIALS AND METHODS

2.1. Scalp Coupling Index (SCI) and Peak Power (PP)

The key objective of our experiments is to measure the coupling strength between the source and the detector optodes of a channel using SCI and the PP as the quantitative measures. fNIRS signals contain the cardiac pulsations which are one among the other systemic noises which should be filtered out to get a noiseless signal. Pulsatile cardiac oscillations represent the blood circulation and physiological factors of the brain, but a strong cardiac pulsation in a signal also signifies a strong link between the emitter and the receiver of a channel [21][22]. Hence the strength of the cardiac oscillations can be used to determine the coupling of a channel, which can be numerically determined as the SCI and PP. This helps to identify optical channels with poor scalp coupling and remove them in experiments involving several optical channels [19].

2.1.1. SCI Computation

SCI is computed as a cross-correlation of the cardiac waveforms collected from two distinct wavelengths of two light signals emitted from a single source of an optical channel. To determine the SCI of a channel, the cardiac pulsations are filtered out from the cortical brain signals and other noises by band-pass filtering the raw intensities between 0.5 Hz and 2.5 Hz that correspond to the heartbeats 30 and 150 beats per minute (bpm). The upper cut-off frequency of the band-pass filter is limited by the Nyquist criterion ($f_{cut\text{-}off} \leq 2 \cdot f_{sampling}$) [19]. The filtered signals are then normalized to their standard deviation to rectify the differences in the amplitudes of the signals at their sources and their extinction coefficient for oxyhemoglobin (Hb) and deoxyhemoglobin (HbR) at the two wavelengths. The similarity between the two cardiac waves is quantified at a time lag of 0. The identical waveforms produced a zero-lag cross-correlation value of 1 and the uncorrelated waveforms gave a value of 0. This correlation value is used as the SCI to quantify the signal to noise ratio of a channel as a numerical measure.

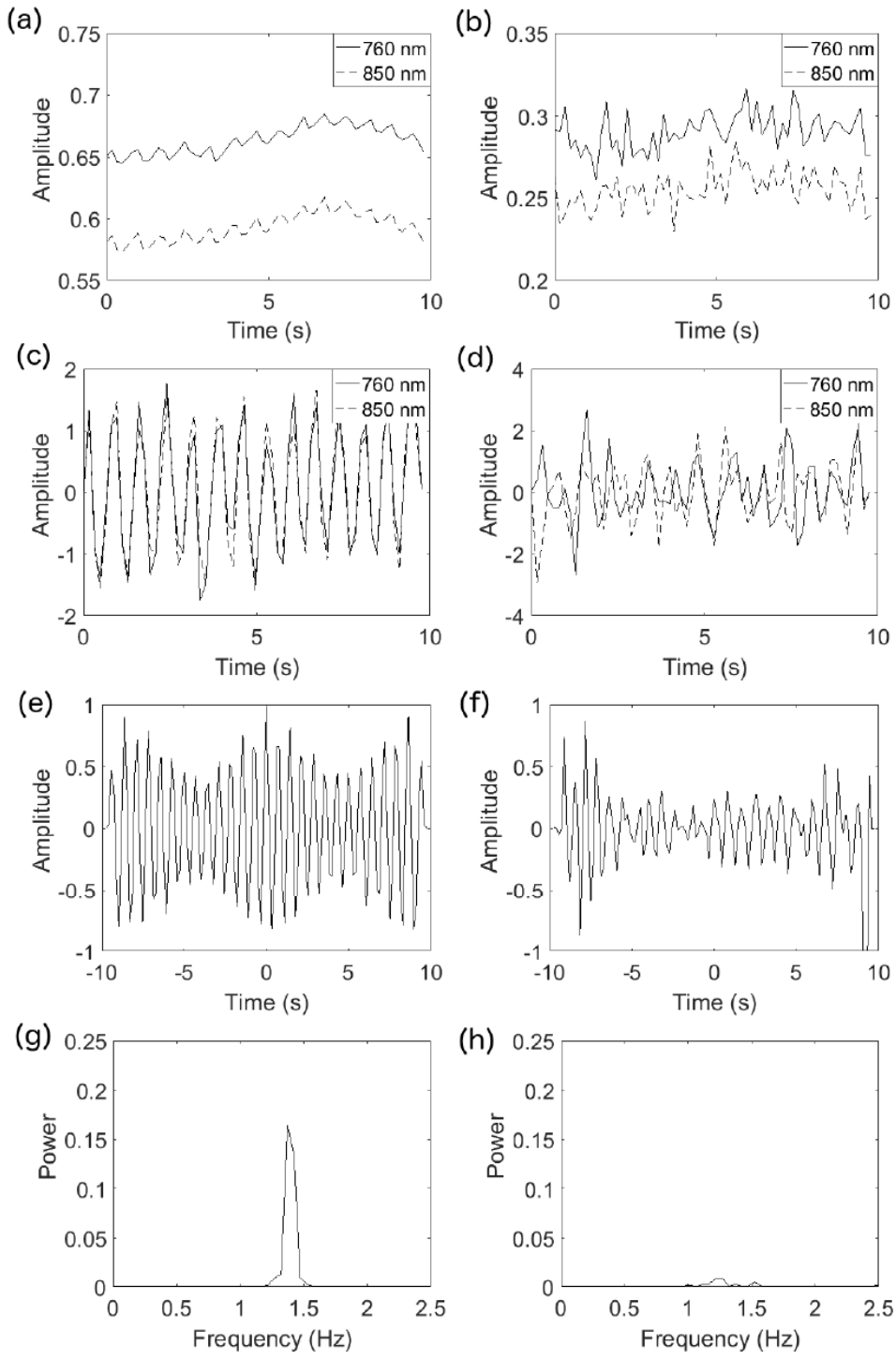

Figure 2 : The Figures on the left represent a channel of clean signal (a). Figures on the right represent a channel of noisy signal (b). The cross-correlation of the wavelengths of (c) the clean channel and (d) noisy channel. The SCI of the both the channels at (e) 1 and (f) 0.23. The PP of the signals at (g) 0.16 and (h) 0.01. As both SCI and PP is good for the clean channel, the coupling strength is indicated as strong. Since the SCI and PP both are low for the other channel, the coupling strength is indicated as weak. The image is taken from [19]

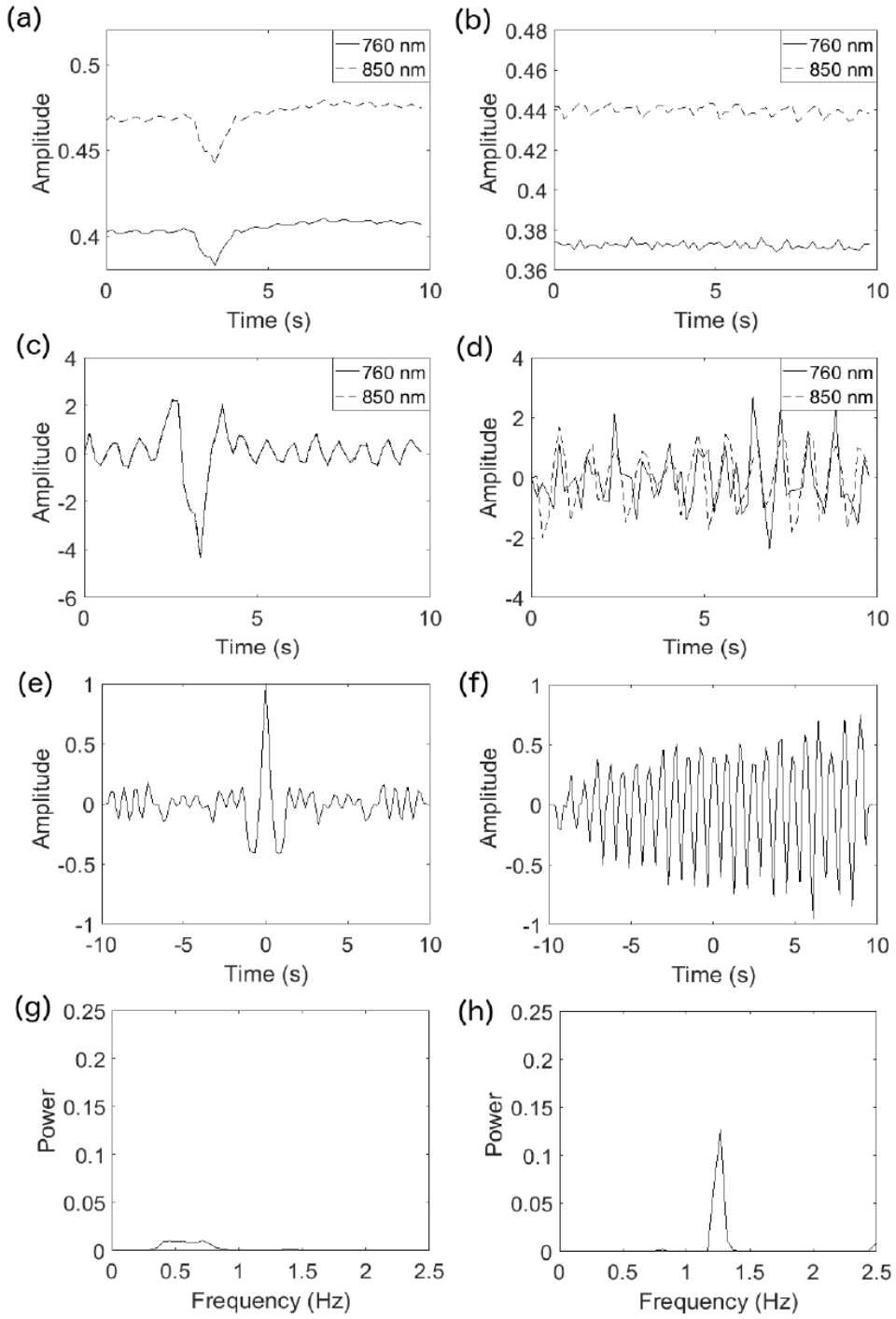

Figure 3 : The Figures on the left represent a channel affected by motion artifact (a). Figures on the right represent a channel of noisy signal at the lower wavelength (b). The cross-correlation of the wavelengths of (c) the motion artifact channel and (d) noisy channel. The SCI of the both the channels at (e) 1 and (f) 0.4. The PP of the signals at (g) 0.01 and (h) 0.15. At least one lower value of SCI or PP in either of the channel indicates that the signal coupling is weak. . The image is taken from [19]

2.1.2. PP Computation

In addition to the SCI, which is derived from the cardiac pulsations, another numerical measure called Peak power is determined which is derived from the additional spectral power features of the cardiac signal [19]. PP helps in the identification of noise due to motion artifacts. Even though fNIRS is more stable to movement artifacts than the other techniques e.g. functional magnetic resonance imaging, electroencephalography/magnetoencephalography (EEG/MEG), signals can still be distorted by head movements, causing fast spikes or shifts from the baseline values. To deal with these motion errors, researchers mostly include the elimination of such signals with the artifacts as a part of pre-processing.

In our experiment, when a motion artifact occurs, both the wavelengths are spiked together, which leads to an erroneously high SCI value, and it should be identified (refer e, f, g, h of the Figure 5). Hence PP is estimated along with the SCI to improve the signal to noise estimation. A single pulse in the middle of the time series, although its location is unimportant, results in a flat power spectral density across the entire frequency range. So, if the data has a strong spike-like motion artifact somewhere, that spike might boost energy level everywhere and make everything else obscure. On the contrary, two pure sinusoidal waves are simulated which oscillates at a frequency at 1 Hz (or 60 bpm) and arbitrary amplitude and offset. The normalized cross-correlation between the signals is computed with an amplitude of 1, frequency f, and the PP of 0.5. When the two wavelengths collected during the experiment are cross correlated, practically they do not provide a PP of 0.5 due to the noises. Hence a threshold value of 0.1 was set which is a fraction of the ideal PP.

2.2. Experimental Protocol

This project was conducted on only one subject and one experimental session lasted no longer than 20 seconds and it is made sure that the signals are collected without any motion artifacts during the time of the data collection. The data is collected from the forehead of the subject seated upright,

and the experimental setup was maintained at a source-detector distance of 7 mm and an integration time of 100 ms. While the other parameters are kept constant, only one of the parameters is varied for the study, for which we measured the intensities of the light detected and the results are recorded for further discussion. The different experimental parameters used for the experiment are discussed in the upcoming sections.

2.3. Experimental Setup

The experimental design consists of

1. Stabilized Fiber-Coupled Tungsten light Source emitting a wide range of illuminating wavelengths ranging from 650 nm to 1040 nm.
2. An emitter which is a flexible fiber optic cable of diameter 400 microns, directs the light to the tissue while another optical fiber of diameter 1000 microns is used as a detector to collect the light diffused by the tissue.
3. The source and the detector fibers are connected to a custom-made probe holder, a minimalistic setup which is a headband with a square piece of plastic with twelve holes made adjacent to each other to hold the optical fibers in place and it can be worn around the head. The experiment is carried out with only a single channel of optical fiber and the headband can be adjusted around the head to place the fibers at different positions of the head.
4. A spectrometer to detect the diffused light as a function of the incident wavelength.

2.3.1. SLS202L Tungsten Light Source

A tungsten light source is a form of an incandescent lamp. During the experiment, a current flow through the Tungsten filament, will heat up to around a couple of thousand Kelvin. Tungsten emanates visible and infrared light at this temperature, creating a light source that can be approximated by a black body radiator. SLS202L is a Tungsten filament light source for IR

applications. It operates at a lower color temperature thus generating more IR output. The filament is sealed behind a Sapphire window which transmits IR, better than quartz. A gold reflector is also placed behind the filament which reflects the longer wavelength thus provide higher output in the NIR to MIR range.

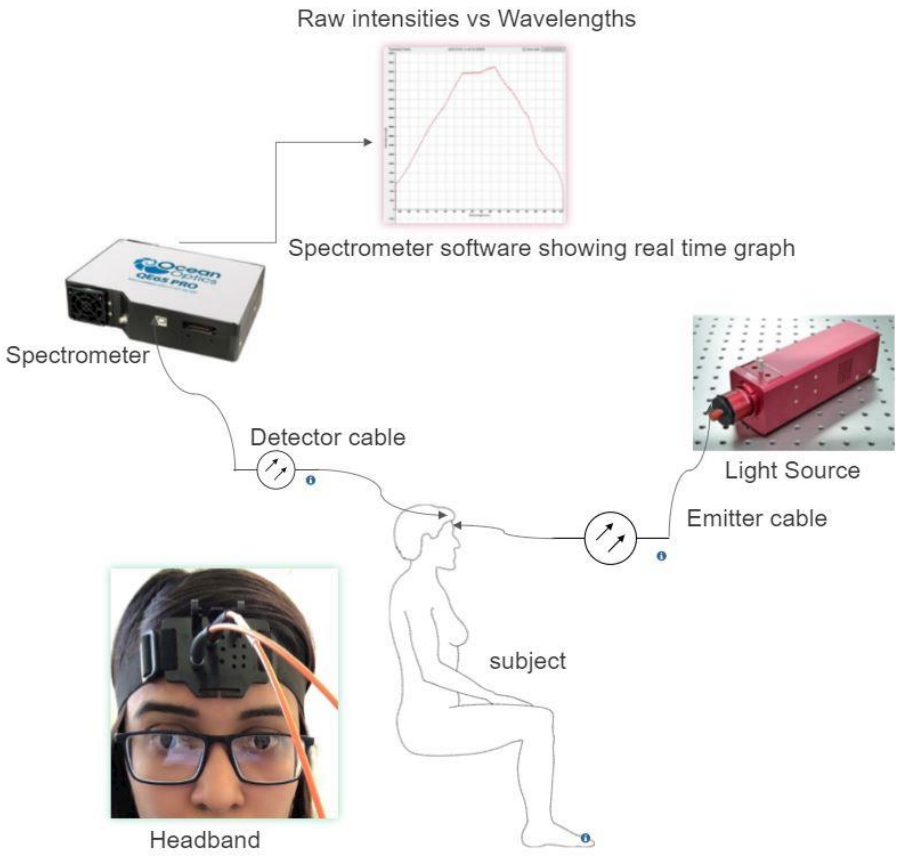

Figure 4: The Experimental design and the head band

2.3.2. Spectrometer

The Ocean Optics QE65 Pro High-Sensitivity Fiber Optic Spectrometer is a scientific-grade spectrometer and its enhanced optical bench provide good performance to improve the response in the NIR regions. The spectrometer produces lower stray light and provides superior dynamic range and high sensitivity for low-light-level applications. So, when the tungsten light source illuminates a broadband spectrum of wavelengths, the light is spatially dispersed over 1044 pixels

of the image sensor. Each pixels measures an intensity. The readouts of the spectrometer is the real time graph showing the intensities as a function of wavelengths along the spectrum.

Figure 4: The Ocean Optics QE65 Pro High-Sensitivity Fiber Optic Spectrometer

The spectrometer software is called Oceanview. This software provides good stability, the persistence of user settings, a broad scope of device features, and consistent file saving and loading procedures. We used the electrical dark-signal correction in our experiment to eliminate the zero-error lighting. The advantage of the software is that real-time display of data allows us to evaluate the effectiveness of our experimental setups and data processing selections, make changes to these parameters, instantly see the effects, and save the data. By using the graph real-time display of data, we can evaluate the effectiveness of the experimental setups and data processing selections, make changes to these parameters instantly see the effects, and save the data. For our experiment, we saved the spectral data in a notepad text file.

2.4. Experimental parameters

This section describes the experimental parameters that we focused in our study to investigate the performance of SCI and PP.

2.4.1. Source-detector distance

The single channel of optical fibers is adjusted by fitting them in the different holes of the square piece in the headband such that the source-detector distances are 7 mm, 13 mm, 22 mm, 30 mm, 32 mm.

2.4.2. Sampling frequency/Integration time

The integration time of the spectrometer is analogous to the shutter speed of a camera. The higher the integration time, the longer the detector monitors the incoming photons. The integration time of light used for the experiment can be changed in acquisition controls of the spectrometer. The data was collected for the integration times of 100 ms, 300 ms, and 500 ms, and their sample frequencies were 10 Hz, 3.33 Hz, and 2 Hz, respectively.

2.4.3. Anatomical location

The third parameter is the anatomical location i.e. the headband is adjusted to different parts of the head and the data is collected from the forehead, right back-head, and left back-head.

2.5. Methods

2.5.1. Wavelength binning

While performing our experiment, the real-time graph in the spectrometer software showed that the time-acquisition function of integrated intensity provides a much clearer cardiac pulsation. But we did not use the time-acquisition function of the spectrometer in our experiment and instead of integrating, we applied the averaging of the data as a part of our post-processing algorithm to have much more control over grouping the number of wavelength pixels data. We did not integrate the intensities as we wanted to retain the values of the intensities. The recorded dataset contains the time-varying intensities of all the wavelengths of the entire spectrum providing 1044 wavelengths between 650 nm to 1021 nm. The intensities of the adjacent wavelength pixels are grouped and averaged to view the cardiac oscillations better. We grouped ten pixels of wavelengths so that 1044 pixels of wavelengths come down to 104 pixels of wavelength. The number of bins to be grouped can be altered as a part of the code.

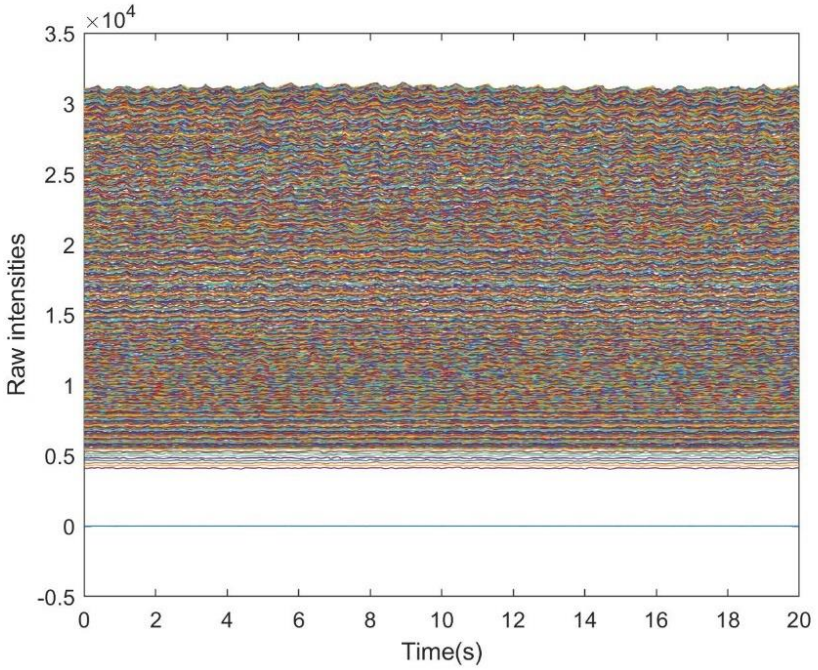

Figure 5.1 : Raw intensities plotted against a spectrum of 1046 wavelengths before binning the adjacent wavelengths

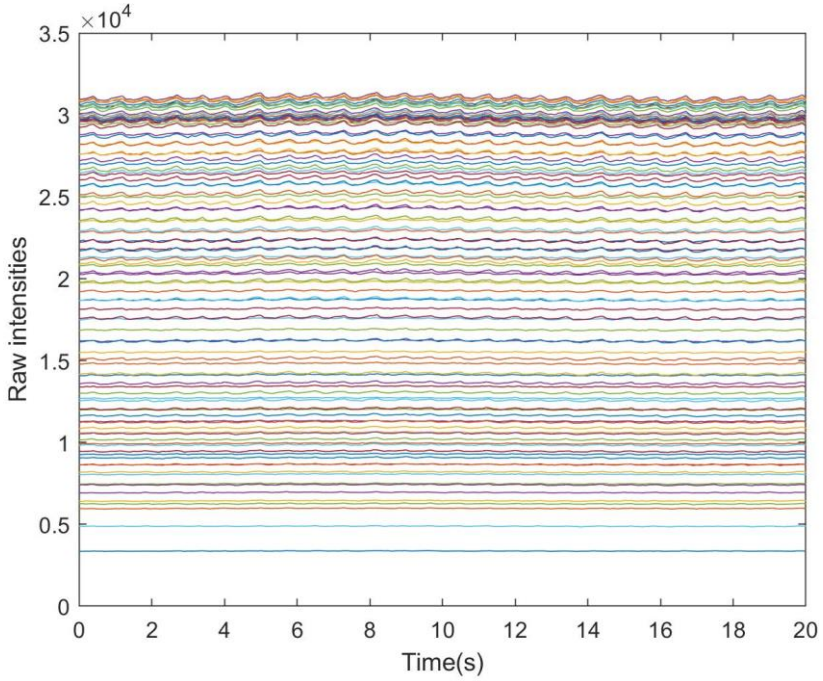

Figure 8.2: After grouping and averaging the raw intensities of adjacent 10 wavelengths , the resulting intensities show clearer periodic cardiac pulsations

2.5.2. Averaging the data using bins of size 'group size' and plotting the bins

For every experimental setup, the raw intensity data are visually inspected using the graphs in the Figures 2.1, 4.1, 5.1, 6.1, 6.2, and 6.3 to assess signals' quality (to see the quasi-sinusoidal nature of the heartbeat oscillations). Based on that the group size is altered, if needed, and then SCI and PP are computed for only a five seconds window. The 20 seconds are divided into 4 windows and the computations are done for each window. When the SCI and PP are computed for shorter windows at a time, movement artifacts can be avoided and they adversely affect the scalp coupling for the entire length of the time window over which SCI and spectral power are computed [19]. We selected the computations from the third windows for further discussions. Hence time course of all the Figures shown belongs to the 3rd window (10th to 15th second) of the entire time frame of 20 seconds.

2.5.3. Computing the SCI, PP in combination metrics

The 104 wavelengths are made into pairs with each other such that there are 5356 combinations of wavelength pairs whose respective SCI and PP values are calculated using the algorithms in MATLAB. The number of adjacent wavelengths grouped to average their intensities(group size) is kept constant as 10, which can also be increased if better cardiac pulsation is needed to be seen in the data for further processing. The resulting wavelengths pairs and their respective SCI and PP are plotted in 3D surface plots.

2.5.4. Tables for wavelengths pairs producing maximum values of SCI and PP

The table given for each parameter is a record of all the maximum values of SCI and PP plotted as a red dot in every SCI or the PP graph. The maximum SCI and the maximum PP from the table for every parameter is given as a recommendation for choosing the wavelength pairs while setting up the experiment to produce maximum SCI and PP.

3. RESULTS

3.1. Source-detector distance

The single channel of the source and the detector optodes are fitted in different holes of the headband to get the different source-detector distances. The short separation distances are 7 mm and 13 mm. The longer separation distances are 22 mm and 32 mm.

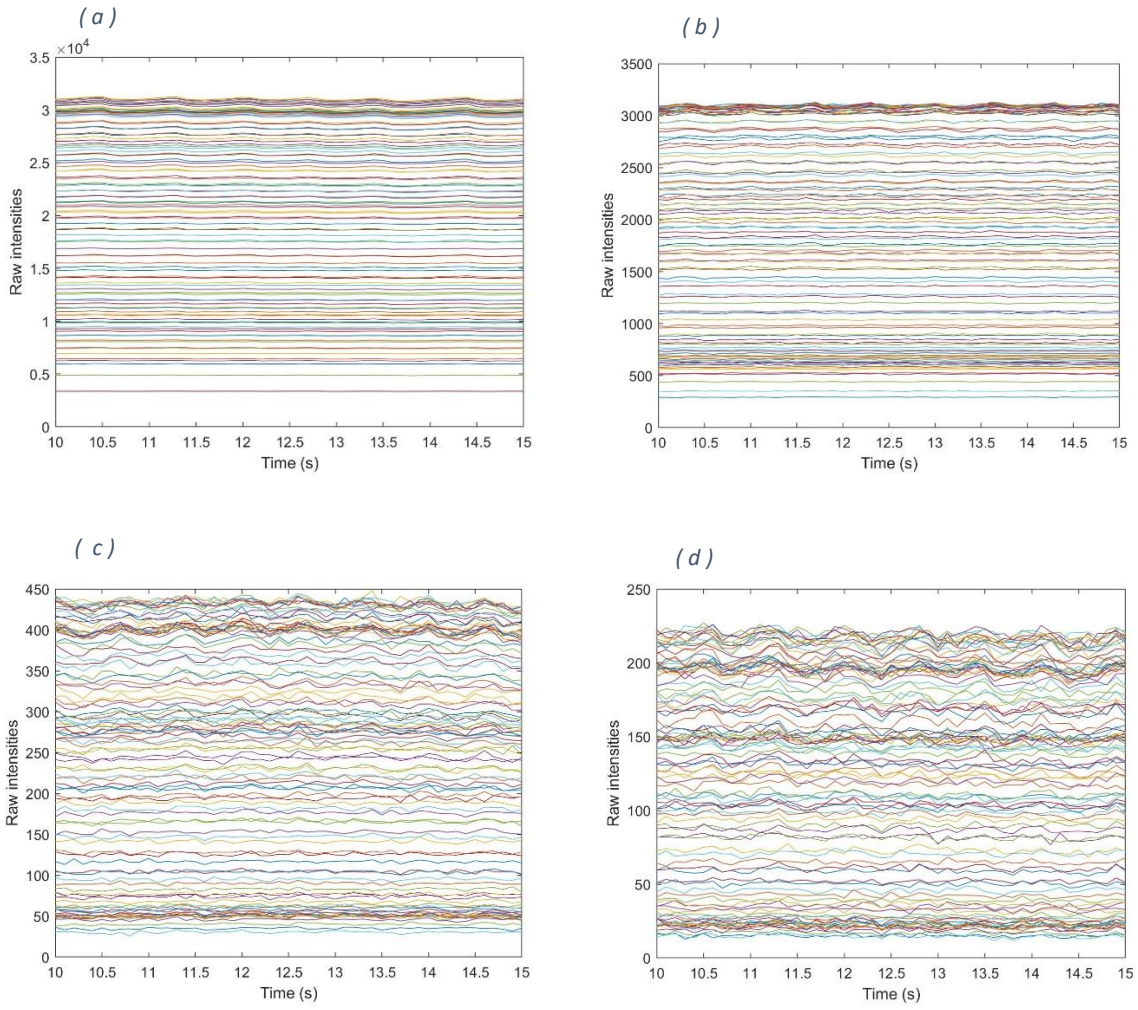

Figure 6.1: *The samples collected for a source-detector distance of (a) 7mm, (b) 13mm , (c)22mm , (d) 32mm . The group size of the wavelengths whose intensities are grouped and averaged is 10 for all the four graphs in the Figure. As we increase the distance, the intensity gets reduced and the quasi-sinusoidal nature of the waveforms becomes deteriorated.*

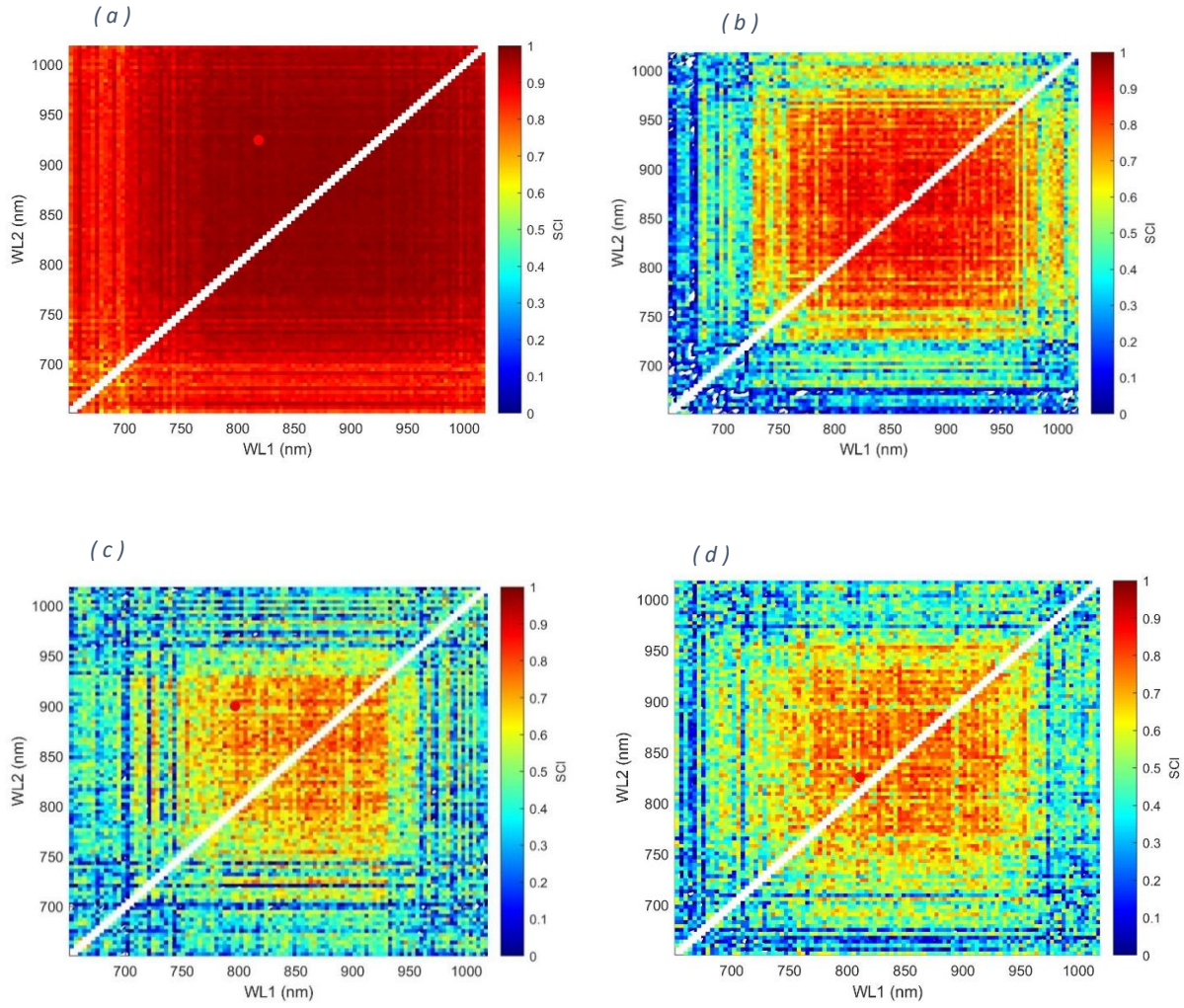

Figure 9.2 : Comparison of the SCI vs the wavelength pairs of the data collected from different distances at (a) 7mm, (b) 13mm , (c)22mm , (d) 32mm. The group size of the wavelengths whose intensities are grouped and averaged is 10 for all the four graphs in the Figure.

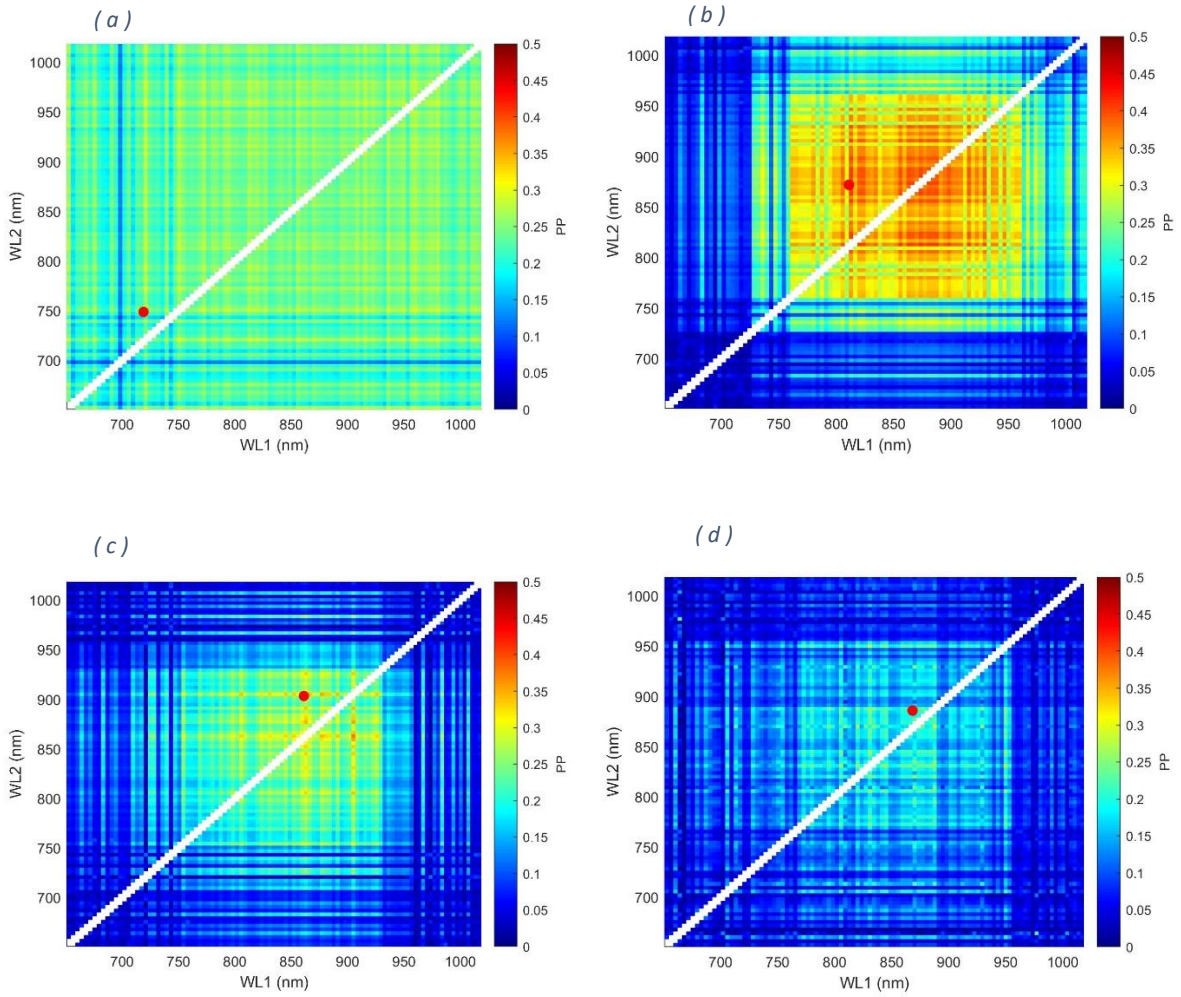

Figure 9.3 : Comparison of the PP vs the wavelength pairs of the data collected from different distances (a) 7mm, (b) 13mm , (c)22mm , (d) 32mm. The group size of the wavelengths whose intensities are grouped and averaged is 10 for all the four graphs in the Figure.

3.1.1. The Zero PP profile of 700.1 nm at the 3rd time window

The Figure 9.3 (a) shows the 3D plot of the PP vs wavelength pairs. We can see that the PP for any wavelength pairing with 700.1nm wavelength gives a value of zero. So, the shape of the 700.1nm wavelength was compared with a few other wavelengths which showed good PP values as seen in the Figure 9.3.

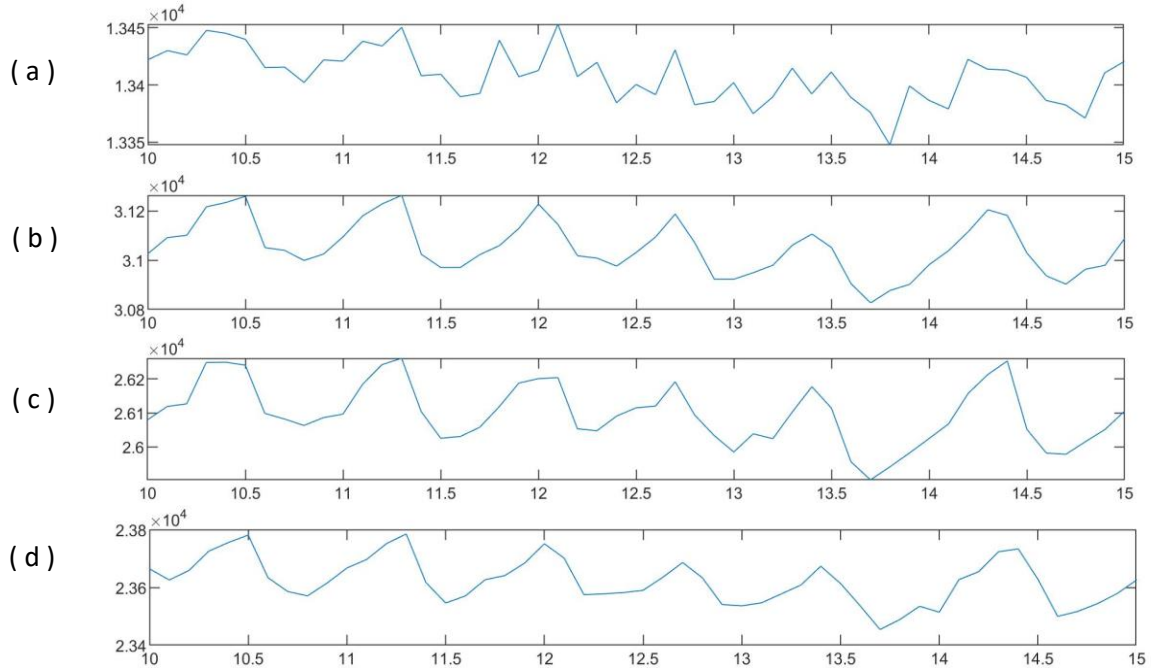

Figure 10.1: From top to bottom showing the waveforms of wavelengths (a) 700.1 nm, (b) 868.2 nm, (c) 903.3 nm, (d) 920.6 nm. These waveforms are taken from the 3rd window which is used for the PP computation.

The Figure 10.1 (a) shows a distorted wave nature, so the PP computation for 700.1nm wavelength paired with and any other wavelength gives a value almost near to zero. This can also be seen in all the PP graphs of other parameters as well. It is mentioned in Dr.Pollonini's research [20] that Since the cardiac component of an fNIRS signal is mostly associated with blood volume changes in the arterial compartment where the fraction of HbR is significantly lower than the fraction of HbO, the cardiac signal measured using near-visible wavelengths (e.g., 685-705 nm) is usually noisier than the cardiac signal measured using longer wavelengths (e.g., 760-780 nm). So, we investigated the wavelength of 700.1 nm across all the four-time windows as shown in the graphs of the Figure 10.2.

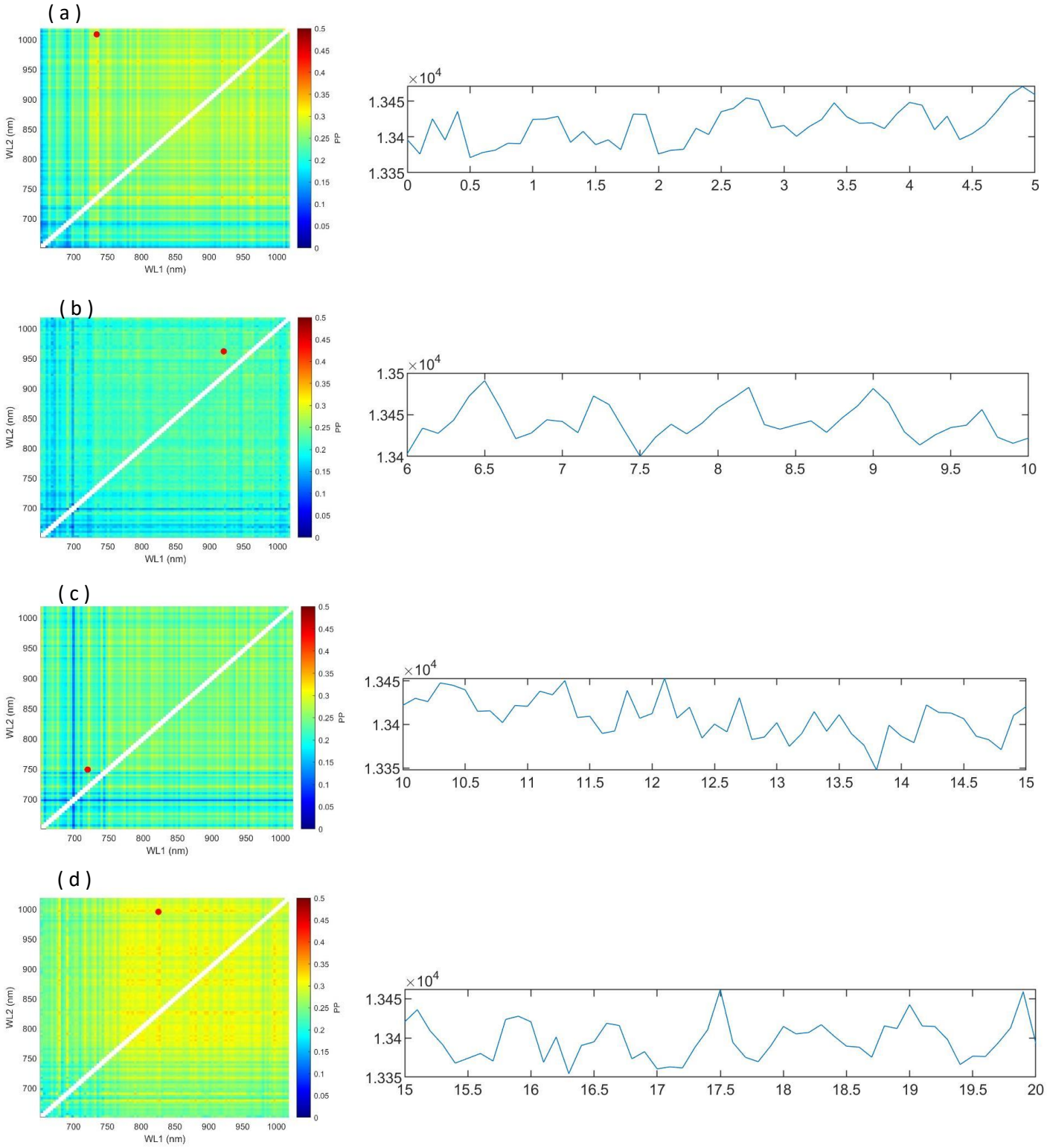

Figure 10.2: To understand more about the PP profile of 700.1nm wavelength , we compared its 3D plot of the PP in the left panel and the corresponding waveform in the right panels across the four-time windows from top to bottom to relate the PP of the wavelengths paired with 700.1 nm and the 700.1 nm wave's shape in a time window.

The distorted nature of the wavelength seems to increase from the first to the third window, but the 3D plot of the fourth window shows that the PP of the wavelength has improved from zero even when the waveform doesn't show a proper periodic oscillation. So, we increased the group size to 30 and checked the improvement of the quasi-sinusoidal form of the 700.1nm wavelength in the third window.

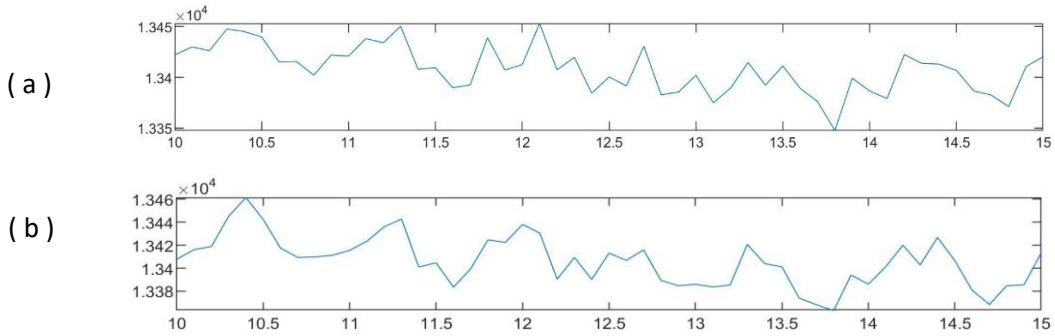

Figure 10.3: (a) Wavelength 700.1 nm with group size of 10, (b) Wavelength 700.1 nm with group size of 30

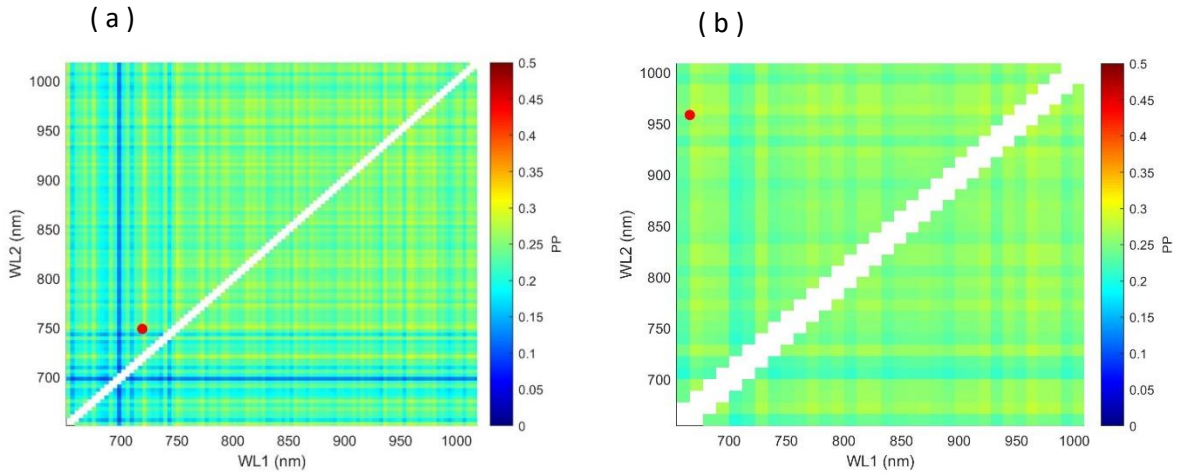

Figure 10.4: (a) PP of 700.1 nm with group size of 10, (b) PP of 700.1 nm with group size of 30

Even after increasing group size to 30, the shape of the wave is improved only a little but still not as good as the quasi-sinusoidal nature as the other three waveforms in the Figure 10 .1 (b) or (c) or (d). But, from the Figures 10.4 (a) and (b), after grouping the wavelengths to a group size of 30, the PP value of 700.1 nm wavelength pairs is no longer 0 but increased to almost 0.2 to 0.3. It is understood that increasing the group size can increase the quasi-sinusoidal nature of the wave and hence the PP is increased from 0.

3.1.2. The effect of group-size on the 32 mm distance

For a longer distance like the 32 mm even after grouping 10 wavelengths' intensities, the data looks noisy and we are not able to view the cardiac oscillations distinctively. Hence the group size is increased, and the results are recorded.

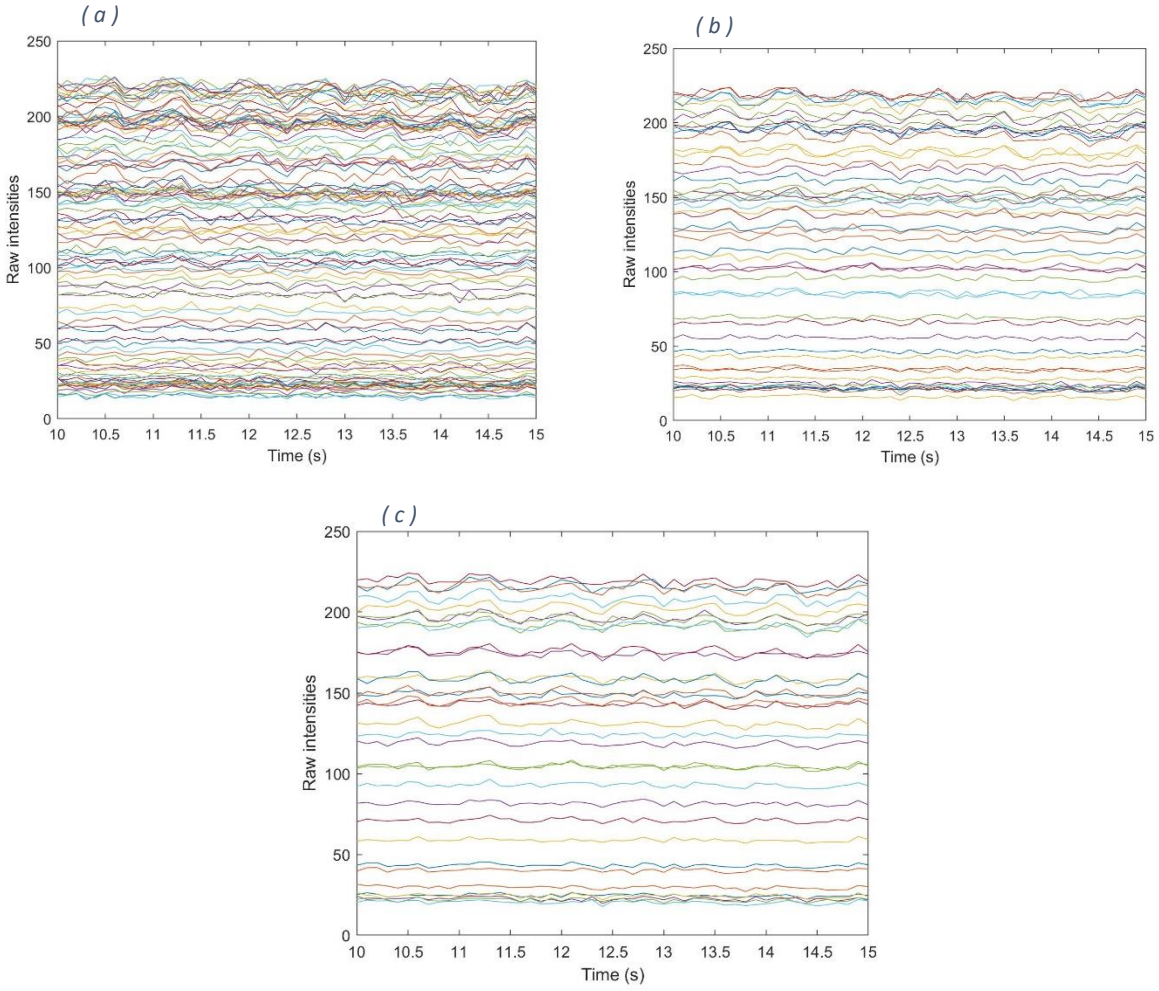

Figure 11.1: The samples collected for a source-detector distance of 32 mm with different group sizes of (a) 10, (b) 20, (c) 30.

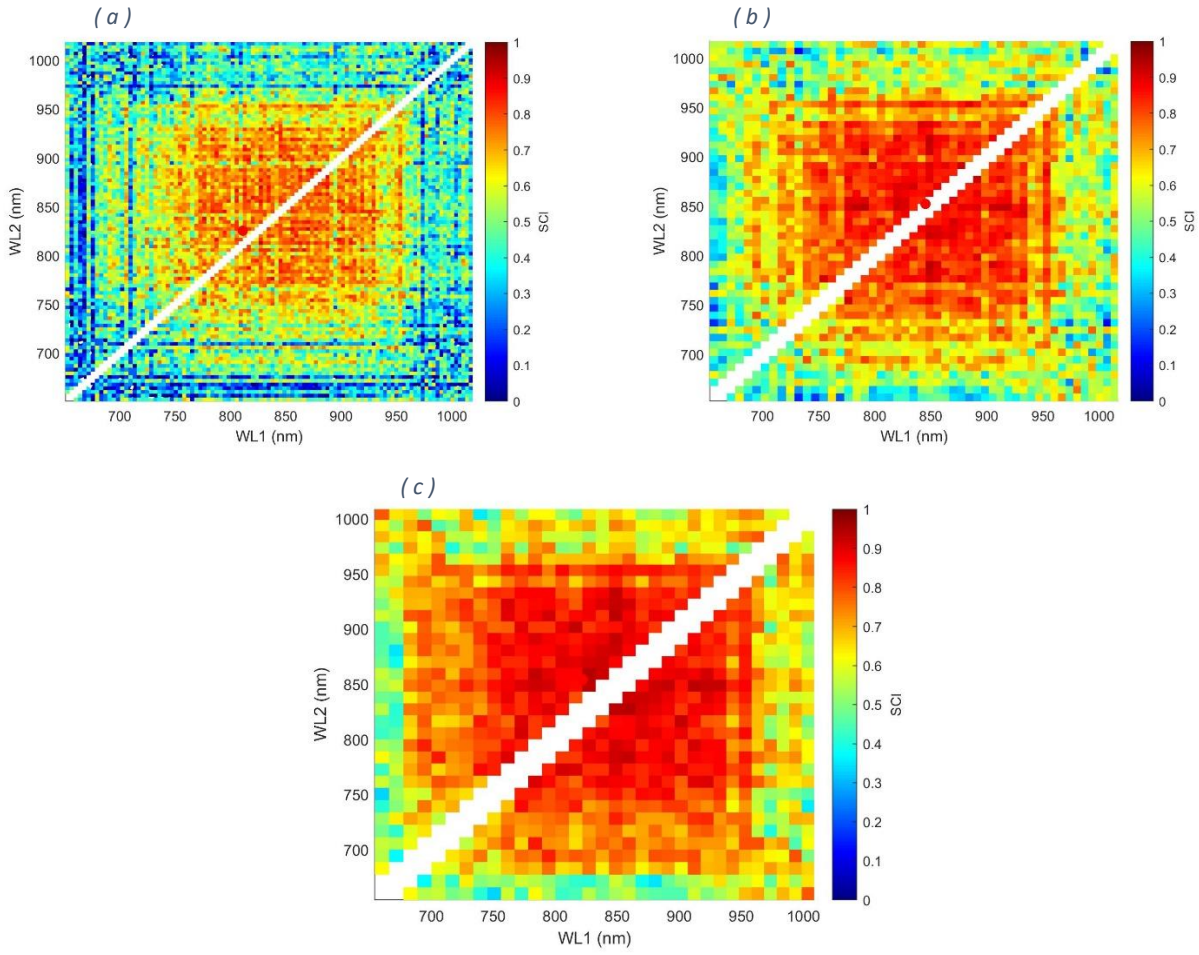

Figure 11.2: Comparison of the SCI vs the wavelength pairs of the data collected for 32mm with different group sizes of (a) 10, (b) 20, (c) 30.

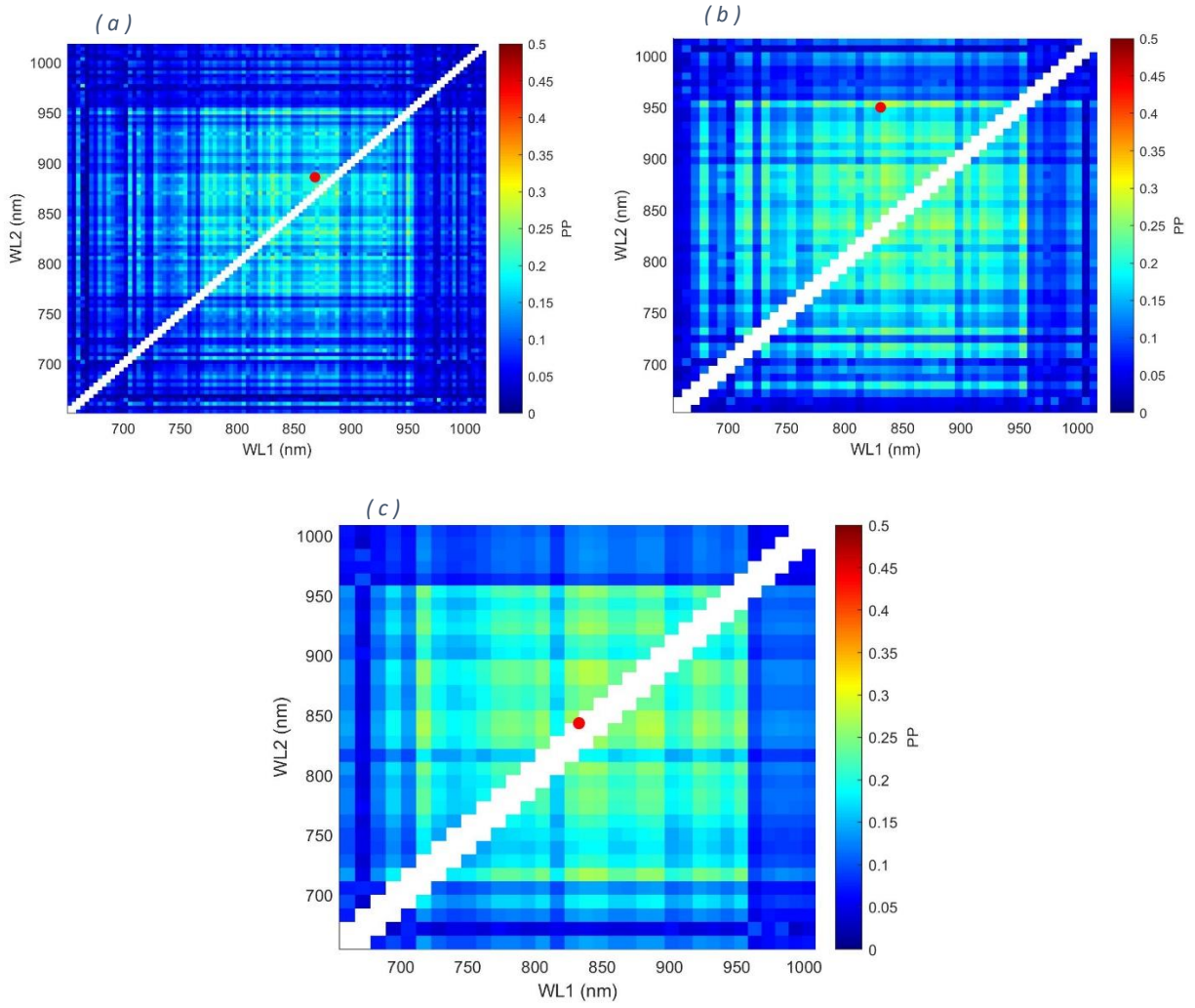

Figure 11.3: Comparison of the PP vs the wavelength pairs of the data collected for a distance of 32mm with different group sizes of (a) 10, (b) 20, (c) 30.

Table 1

The wavelength pairs which produce the maximum SCI and maximum PP with their respective source-detector distance and the group size .

Distance (mm)		Maximum SCI	Wavelength pair for Max SCI (nm)	Maximum PP	Wavelength pair for Maximum PP (nm)
7		0.9939	818.23 924.11	0.3029	718.94 748.75
13		0.9538	864.70 871.77	0.4124	811.00 871.77
22		0.8972	796.49 899.83	0.3786	861.15 903.32
32	Group size : 10	0.9279	811.00 825.44	0.2924	868.23 885.84
	20	0.9380	845.15 852.27	0.2886	830.83 949.83
	30	0.9424	821.84 854.05	0.2798	832.62 843.36

3.2. Integration time

Keeping the distance constant at 10 mm, the second parameter that we change is the integration time in the acquisition controls of the spectrometer. This, in turn, alters the sampling frequency of the data. We collected the data for integration times of 100ms, 300ms, and 500ms for the same distance.

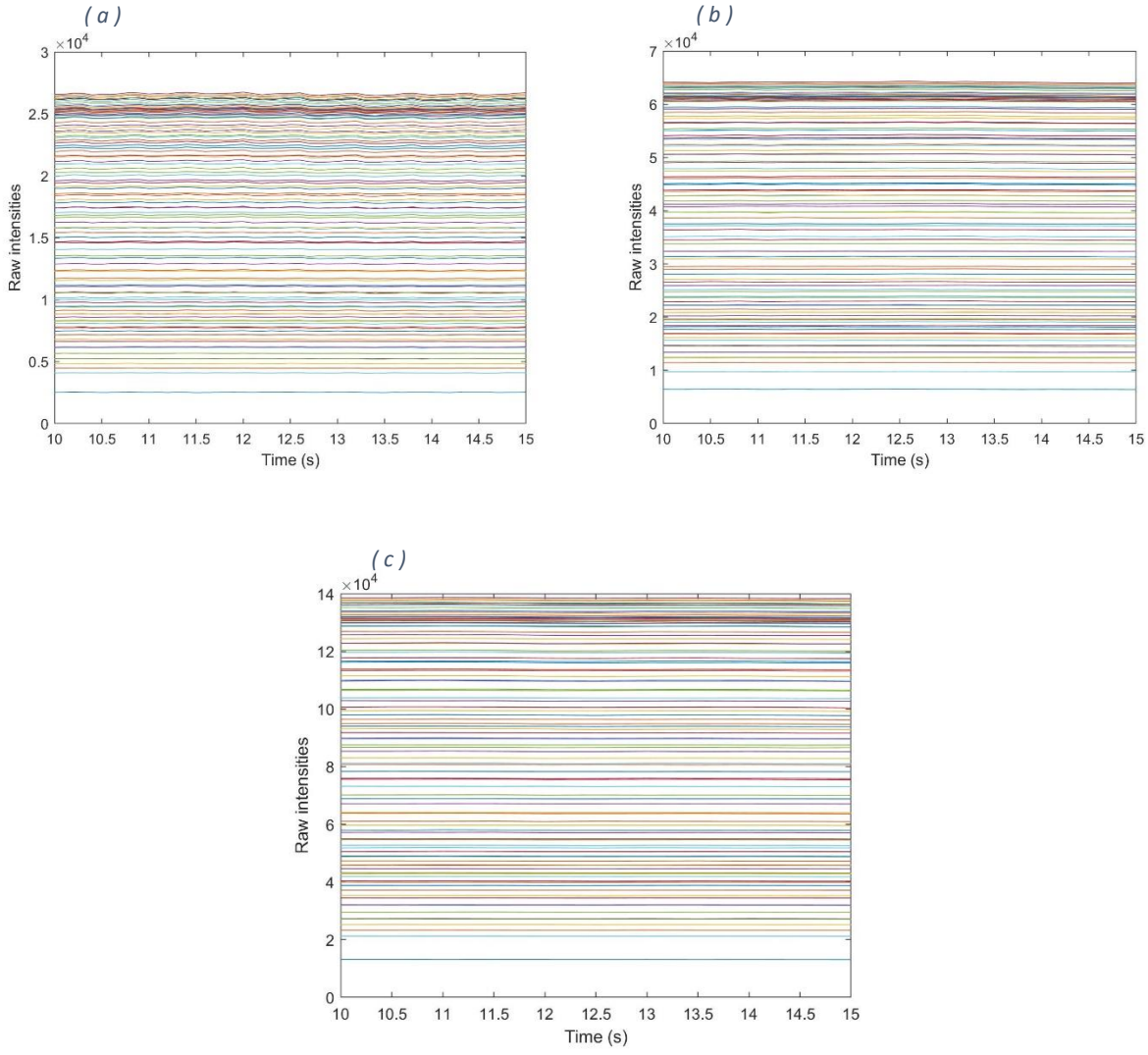

Figure 12.1: This graph shows the shape of the waves collected for different integration times of (a) 100ms , (b) 300ms ,(c) 500ms.

From the graphs above, we can see that the intensities become high when the integration times are increased, and the shape of the waves are flattened out.

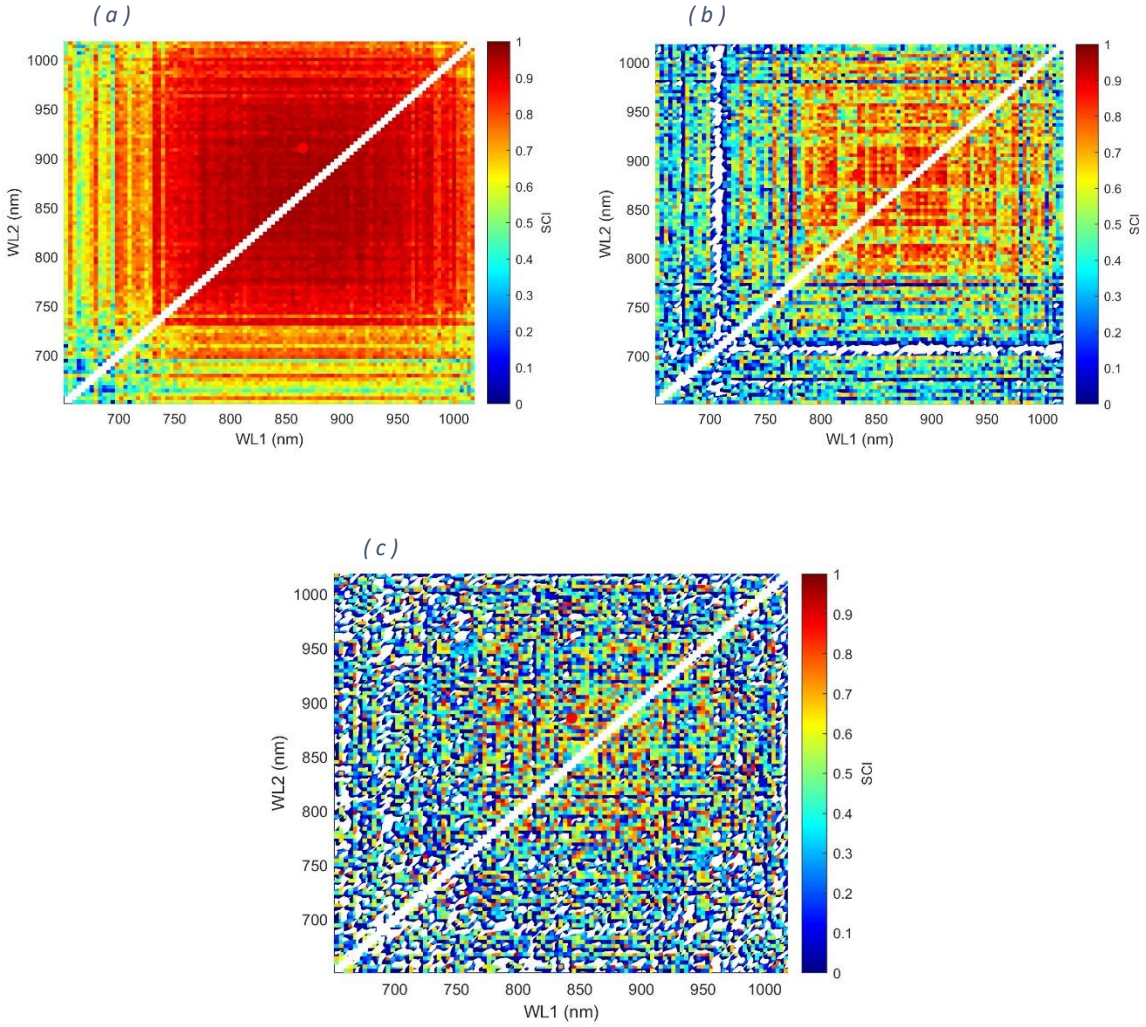

Figure 12.2: Comparison of the SCI vs the wavelength pairs of the data collected for different integration times of (a) 100ms , (b) 300ms ,(c) 500ms.

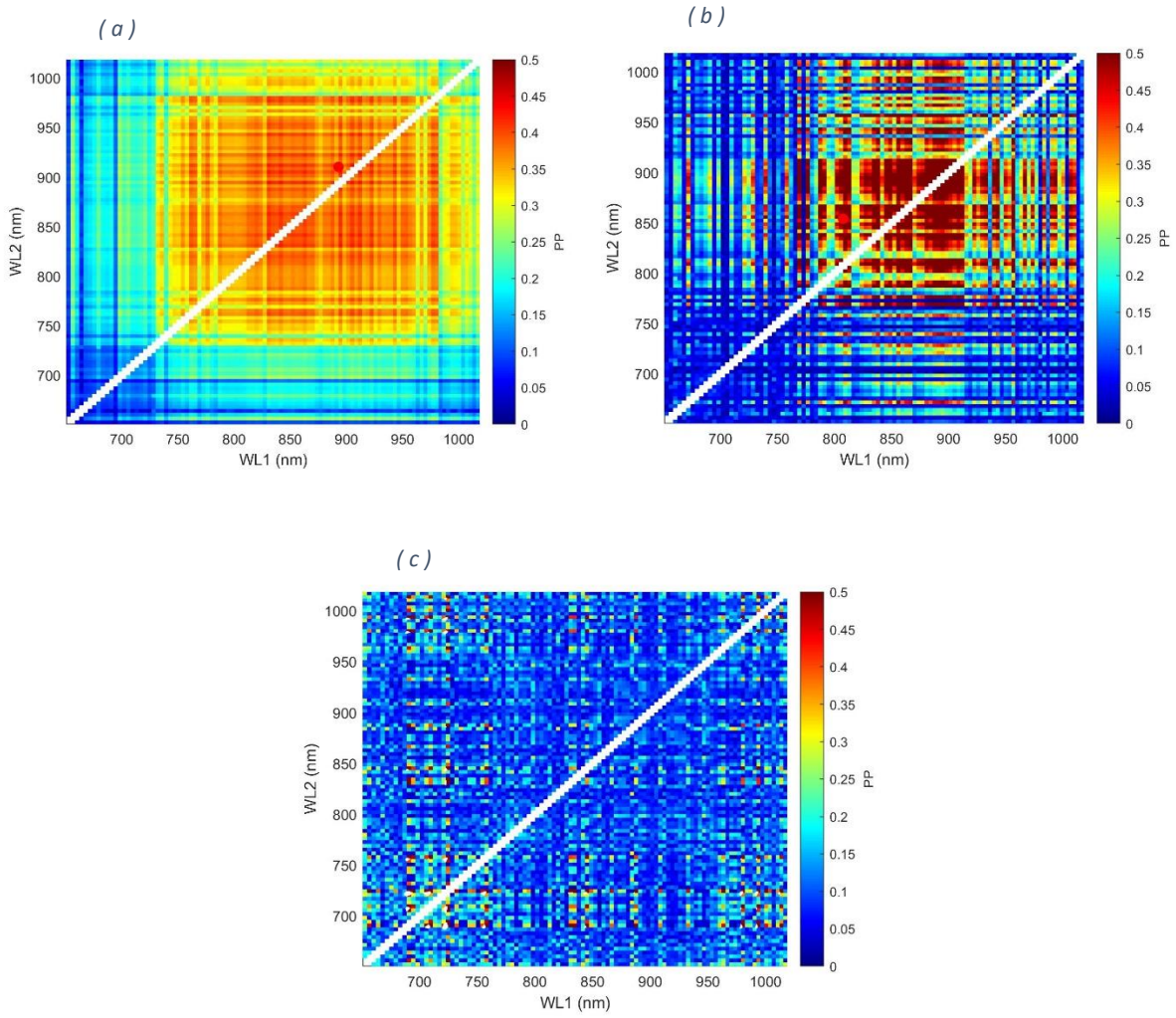

Figure 12.3: Comparison of the PP vs the wavelength pairs of the data collected for different integration times of (a) 100ms , (b) 300ms ,(c) 500ms.

Table 2

The wavelength pairs which produce the maximum SCI and maximum PP with their respective integration time and sample frequency

Integration time (ms)	Sampling Frequency (Hz)	Maximum SCI	Wavelength pair for Max SCI (nm)	Maximum PP	Wavelength pair for Maximum PP (nm)
100	10	0.9804	864.70 910.27	0.4285	892.85 910.27
300	3.33	0.9492	832.62 885.84	0.8938	807.38 854.05
500	2	0.9601	843.36 885.84	0.9928	688.81 722.68

3.3. Anatomical Locations of the head

Keeping the distance constant at 7 mm, the samples are collected from different anatomical locations of the head. The group sizes are increased when the samples are collected from the temporal areas of the head.

The cortex, or cerebrum, is the largest part of the brain. It is divided into two halves, or hemispheres — the right brain and the left brain. Each brain hemisphere is also divided into four sections, known as lobes. The prefrontal cortex is a part of the brain located at the front of the frontal lobe. It is involved in a variety of complex behaviors, including planning, and contributes to the personality development. We collected the forehead data from this part of the brain.

3.3.1. Forehead

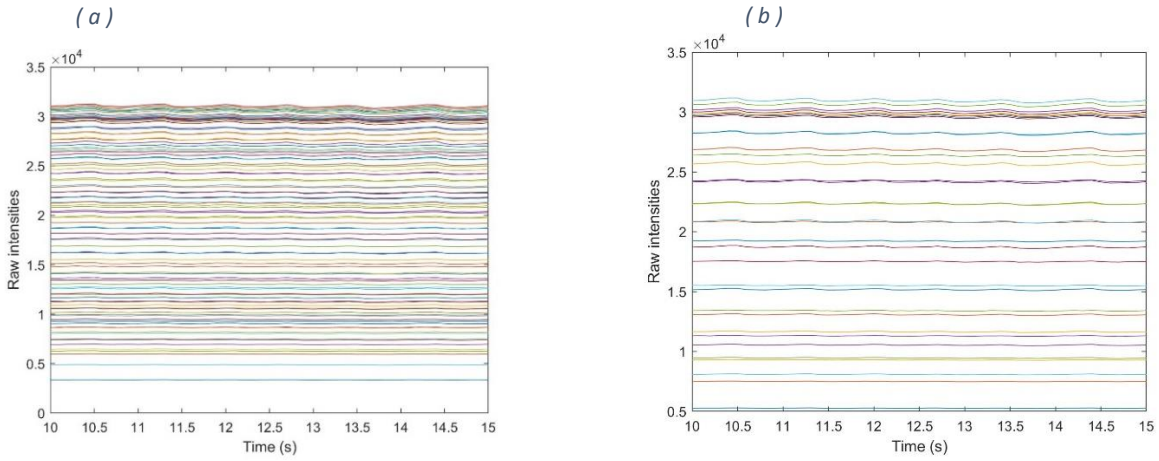

Figure 13.1: This graph shows the shape of the waves collected from the forehead , with a group size of (a) 10, (b) 30.

The second-largest lobe is called the temporal lobe which is located behind the ears. They help to process auditory information, emotions, language, visual perception, and the encoding of memory. We collected the left back-head data from this part of the brain which is the dominant side of the temporal lobe. It helps with learning and remembering verbal information.

The creative side of the temporal lobe is in the right side which helps in learning and remembering visually understandable information like body language, music, and arts. We collected the right back-head data from this part of the brain.

3.3.2. Left back-head

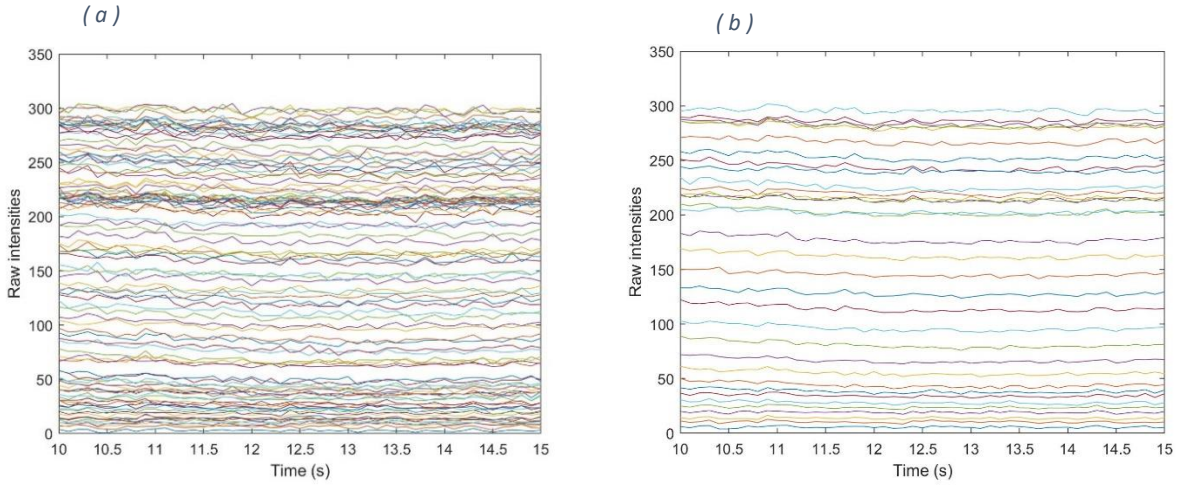

Figure 13.2: This graph shows the shape of waves collected from the left backside of the head , with a group size of (a) 10, (b) 30.

3.3.3. Right back-head

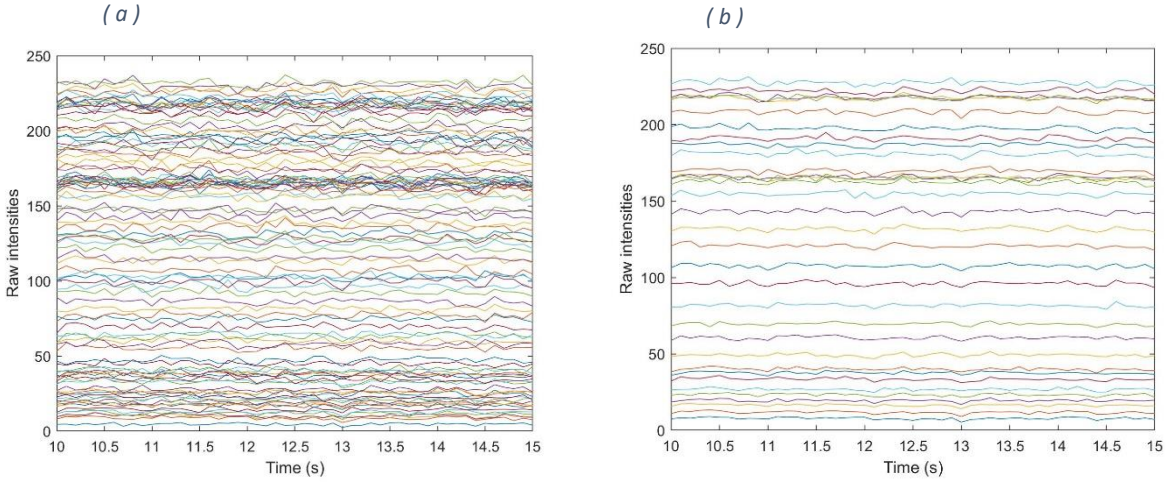

Figure 13.3: This graph shows the shape of waves collected from the right backside of the head , with a group size of (a) 10, (b) 30.

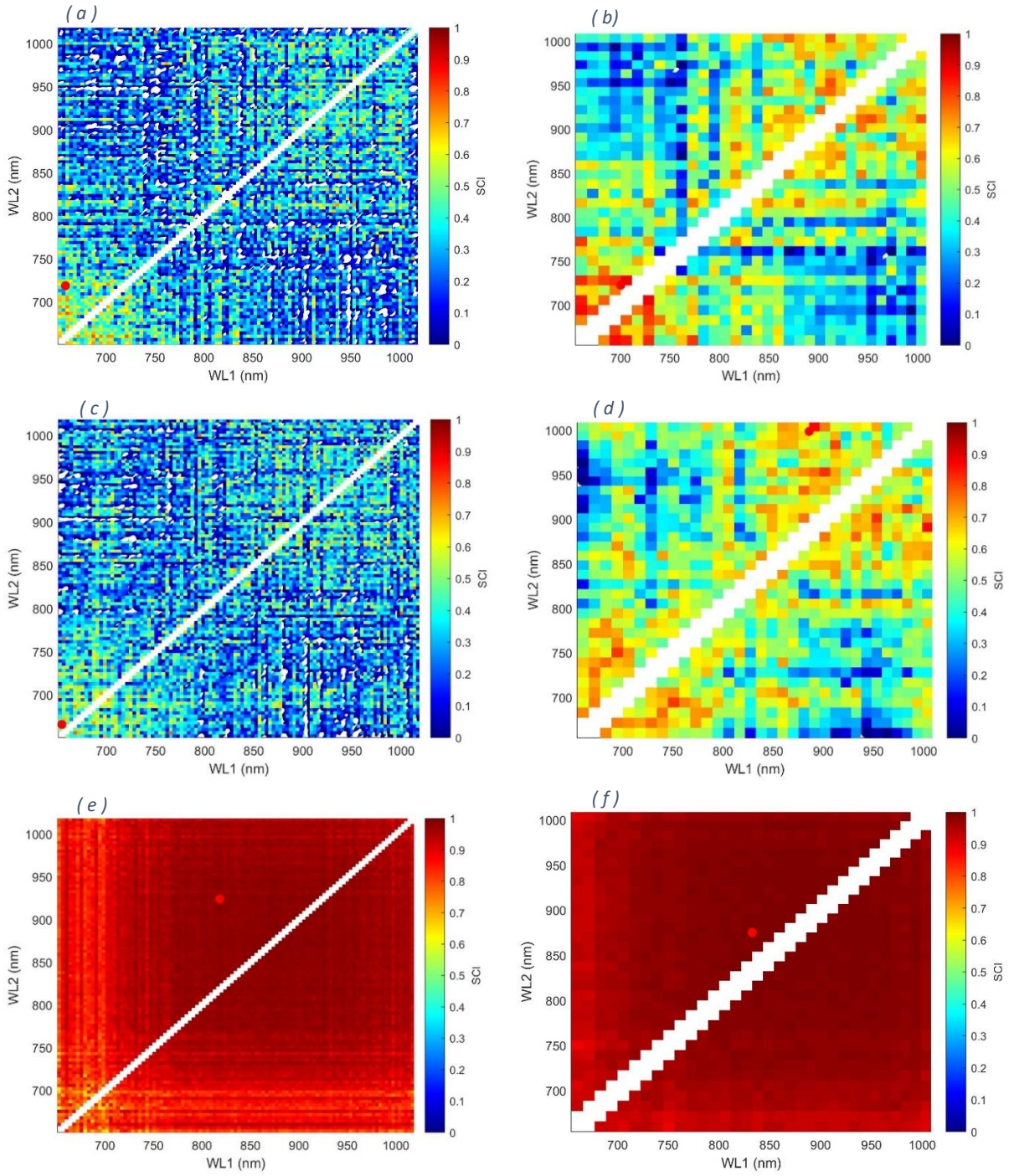

Figure 13.4: Comparison of the SCI vs the wavelength pairs of the data collected from different locations of the head with different group sizes at (a) left back-head group size 10, (b) left back-head group size 30, (c) right back-head group size 10, (d) left back-head group size 30, (e) forehead group size 10, (f) forehead group size 30.

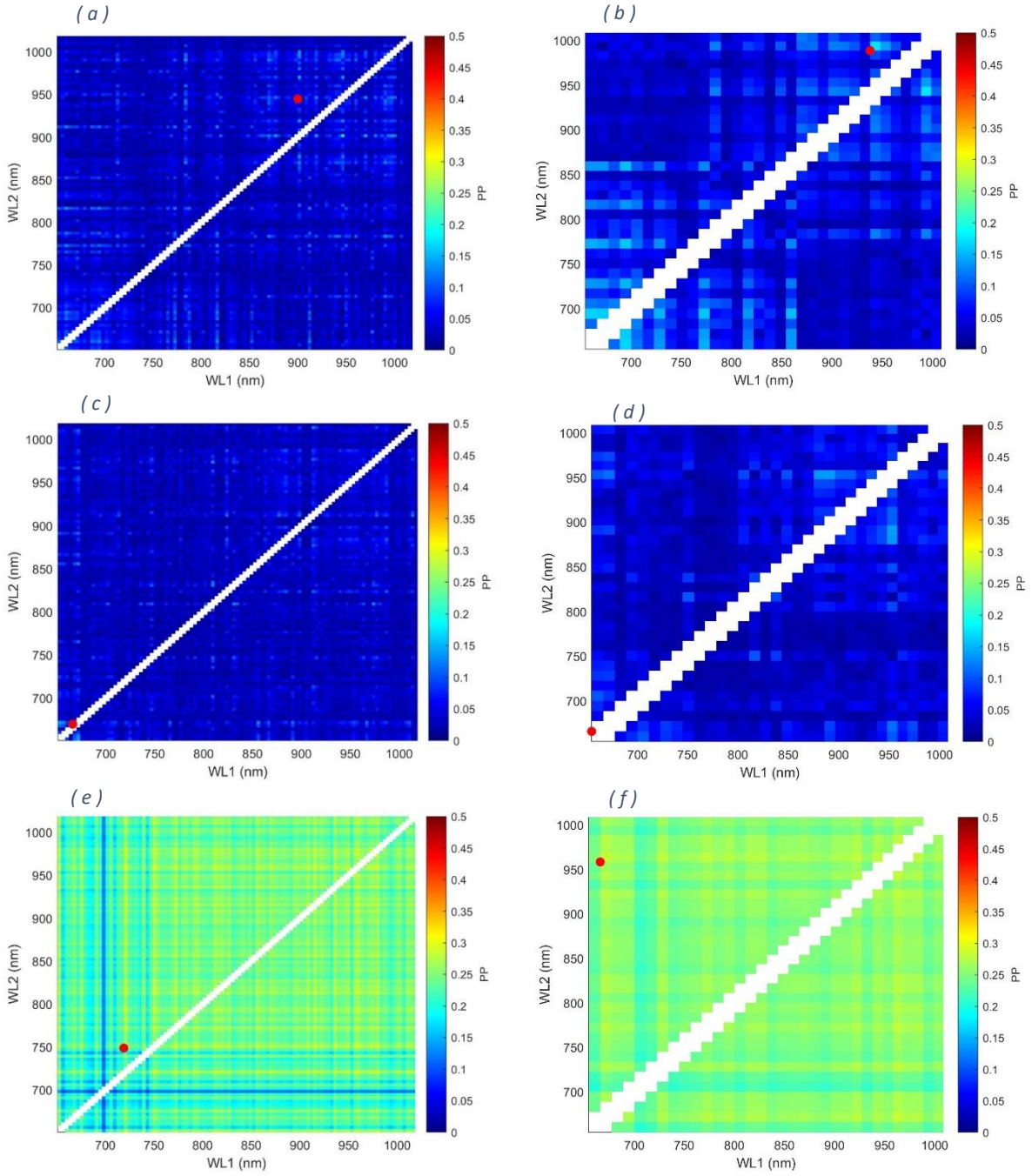

Figure 13.5: Comparison of the PP vs the wavelength pairs of the data collected from different locations of the head with different group sizes at (a) left back-head group size 10, (b) left back-head group size 30, (c) right back-head group size 10, (d) left back-head group size 30, (e) forehead group size 10, (f) forehead group size 30.

Table 3

The wavelength pairs which produce the maximum SCI and maximum PP with their respective anatomical location of the head and the group size.

Anatomical locations of the Head	Group size	Maximum SCI	Wavelength pair for Max SCI (nm)	Maximum PP	Wavelength pair for Maximum PP (nm)
Left back-head	**10**	0.7882	658.36 718.94	0.1820	899.83 944.71
	30	0.8806	700.14 722.68	0.1747	937.86 988.67
Right back-head	**10**	0.7781	654.53 666.00	0.1439	666.00 669.82
	30	0.8629	885.84 998.68	0.1585	654.53 666.00
Forehead	**10**	0.9939	818.23 924.11	0.3029	718.94 748.75
	30	0.9965	832.62 875.29	0.2828	666.00 958.33

4. DISCUSSION

It is essential to quantify the quality of fNIRS measurements using SCI and PP because, they help in indicating the coupling strength of the optodes with the help of the strong cardiac signals. The 3D graphs of SCI and PP vs the wavelength pairs for every case of the parameter are studied individually and then compared with the graphs of other cases of the parameter to study the effect of the parameter on the SCI and the PP.

4.1. Source detector distance

The Figure 9.2 (a) shows that for 7mm source-detector distance, almost all the wavelength pairs produce high SCI from 0.8 to 1. And in the Figure 9.2 (b), for a 13mm source-detector distance, the SCI is high for wavelength pairs in the range 750nm to 950nm. It is reported in previous research that a 6 mm separation results in better contrast-to-noise of functional responses than a 13 mm separation and suggested this was due to the non-negligible brain sensitivity of a 13 mm channel [26]. Hence 7 mm source-detector has wavelength pairs producing SCI higher than other distances due to the better CNR which produces high correlations between the wavelength pairs.

However, the Figure 9.3 (b) shows, 13mm distance having some wavelength pairs with PP higher than that of the 7mm in the Figure 9.3(a). This could be related to the short separation (SS) channels that are used as regressors to detect signals, mainly sensitive to the superficial layers of the brain while also being insensitive to the deeper brain [22]. The longer separation channels are used to collect the brain signals that are important to study the cortical activity. As the SS channels measure the same superficial hemodynamics as the standard longer separation channels (3 cm), they help in removing the systemic interference that contributes to 60% of the hemoglobin changes present in longer separation measurements [21].

It is found that the optimum SS in the adult is reported to be 8.4 mm [22] from multiple studies that have demonstrated the benefit of SS channels between 5 and 13 mm [21][23][24][25], so the

distance should be a little more than 7 mm for obtaining optimum signals . This can be a reason why most of the PP of 7 mm is of the range 0.25 to 0.3, while for 13 mm distance, the wavelengths pairs in the center of the graph showing higher PP up to 0.4. This shows that even when the wavelength pairs of 7 mm have better correlation than 13 mm, the PP of the signal strength of wavelength pairs of 13 mm is better than that of 7 mm.

Comparison of the long separation distances of 22 mm and 32 mm from the Figures 9.2 and 9.3 shows that the SCI of the wavelength pairs in the center of the 32 mm distance graph is more than that of 22 mm. This could be in line with the research where it is reported that brain sensitivity in the adult increases with increasing source-detector separation up to 32 mm [22]. Table 1 shows that the maximum SCI attained for decrease as we increase the distance between the source and the detector from 7 mm to 22 mm. However, the 22 mm has PP values in the center which are higher than 32 mm.

4.1.1. Effect of group size on the longest distance

Increasing the distance between the source and detector of near-infrared light will generally increase the proportion of detected photons that have traveled through deeper tissues, thus increasing the sensitivity of that channel to the brain. However, this increase in sensitivity to deeper tissues is at the expense of a lower signal-to-noise ratio (SNR) in the measured signal, simply because fewer photons will make it to the detector, per unit time, without being absorbed [22].
When the group size is increased, the number of adjacent wavelengths' intensities are averaged.
From the Figures 11.2 and 11.3, it can be understood that for the longest distance separation of 32mm, when the group size of the number of wavelengths is increased, the respective SCI and PP signals of the wavelength's pairs are increased. After increasing the group size to 30, the maximum SCI reached is around 0.94 which shows the effect of group size on the SCI. Hence group size plays an important role in getting better cardiac oscillations in the data which are useful for computing the SCI and PP measures, which can be used compare, analyze, and give a better judgment for the quality among different data with the same group size.

4.2. Sample frequencies and the integration time of data acquisition

The integration time changes the sampling frequency of the data acquisition. The graphs in the Figure 12.2 shows that the number of wavelength pairs producing the strongest SCI decreases and there are a lot of null values as we increase the integration time. Also, if we look at the PP values in Table 2 to check if the SCI values are reliable, the integration times of 300ms and 500ms shows PP values of 0.8938 and 0.9928 respectively which are beyond 0.5 which is ideal PP of a pure sinusoidal signal. So, both the SCI and PP computations for such frequencies provide incorrect results.

As we increase the integration time, the sampling frequency becomes less. For an integration time of 100 ms, the sampling frequency is 10 Hz, but when we increase the integration time to 300 ms, 3.333 samples are collected per second and for 500 ms, only 2 samples are collected per second So, the high pass cutoff frequency of the bandpass filter is reduced from 2.5 Hz to 1.6667 Hz for an integration time of 300 ms, and from 2.5 Hz to 1 Hz for 500 ms, to satisfy the Nyquist sampling criterion. The ideal cut-off frequencies of the bandpass filter set for the experiment are. So, when the integration time is increased beyond 200 ms (5 Hz), the sampling rate starts going lower than 5 Hz. Hence this kind of down-sampling can introduce a form of distortion in the data called aliasing, especially at the high-frequencies and when the new sampling rate is smaller than twice the highest frequency of interest in the signal (Nyquist frequency) [27].

Data sampling below the Nyquist frequency regarding the frequency of cardiac and respiratory processes causes aliasing artifacts in the image data, which have been a persistent source of uncertainty in functional analyses [13]. For 300ms and 500ms integration times, the sampling frequency is quite small, then the quality evaluation is performed over a kind of "triangular" signal. Even if there is a cardiac pulsation is present in the data, the sampling frequency is so small that instead of generating a sort of sinusoidal signal, the filtered version of the data generates a kind of triangular wave (Figure 14). Due to the extreme PP produced at that a low frequency, the PP values are falsely reported which also shows that the SCI values are incorrect too.

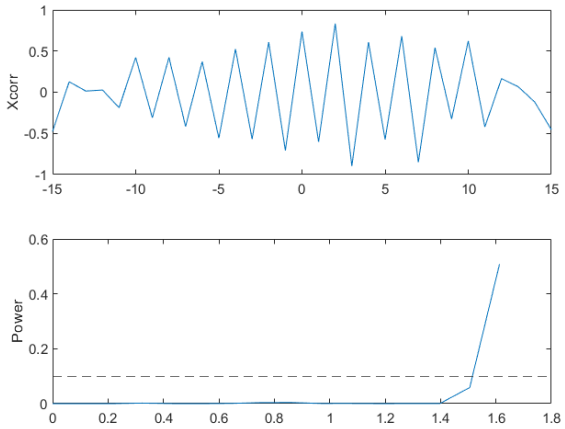

Figure 14: The PP computation providing the higher value which is incorrect as the correlation is computed over triangular signals instead of the quasi-sinusoidal signals

4.3. Anatomical position of the head

Since the forehead is the non-hairy part of the head, the detected signals have high intensities and the SCI and PP are better than the signals collected from any other part of the head. To compare the data collected from the right and left back-head which are the locations of the head obstructed by hair, we examined their SCI and PP graphs. The Figure 13.4 shows that the values of SCI in the graphs for the group size of 30 are much clearer than the SCI values in the graphs of group size 10 for both left and right data. However, from the Figure 13.5 (b) and 13.5 (c), the PP of the signals seems to have improved very little only for a few wavelengths even after grouping. Hence to study signals from the temporal regions of the head, a group size of 30 provides a clearer data which can be used for comparing the quality of data using SCI and PP.

To learn more about these wavelengths, we investigated the timestamp graphs (Figure 15) from the Oceanview spectrometer software, which is a real-time graph showing intensities vs wavelengths collected during the time of data collection. The intensities are so high for the signals collected from the forehead, which goes up to 3000. The highest intensity for the left back-head is 330 and for the right back-head 250 which a little lesser than left back-head. The right back-head

signals look noisier than the left back-head. This is backed by the Figures 13.5 (b) and 13.5 (c) which shows that the PP of left back-head is little better than the right back-head before and after grouping. This can be supported from the values of SCI and PP from Table 3.

We can also see from the Figures below that the wavelengths peaks for the forehead at 800 nm to 900 nm. This is the same for all the data collected from the forehead for all the different parameters (source-distance, integration times). This is different from the wavelength peaks of left and right back-head which is around 880 nm to 950 nm. So, these wavelengths can be used to collect better signals for experiments required to collect from the temporal regions of the head.

(a)

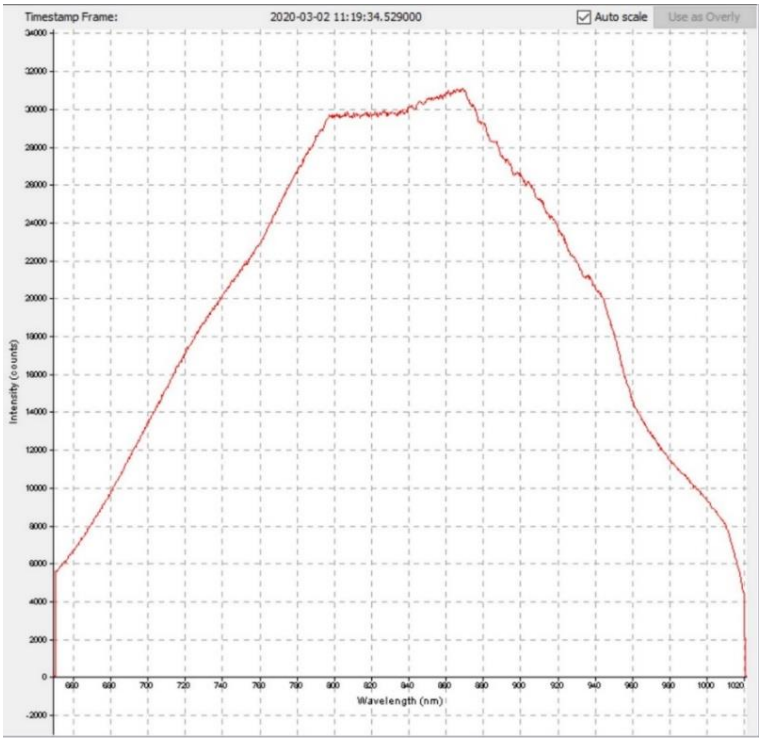

(b)

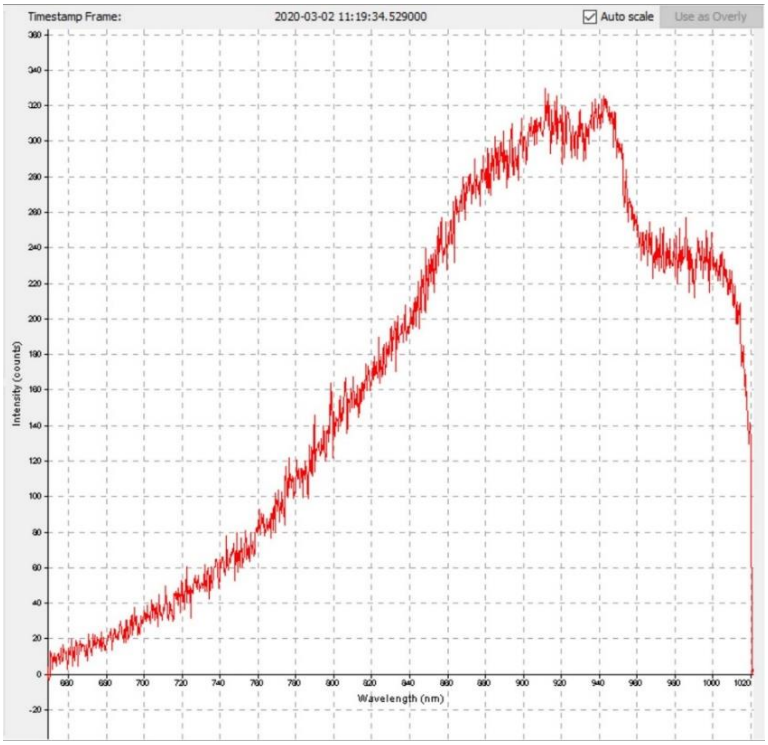

(c)

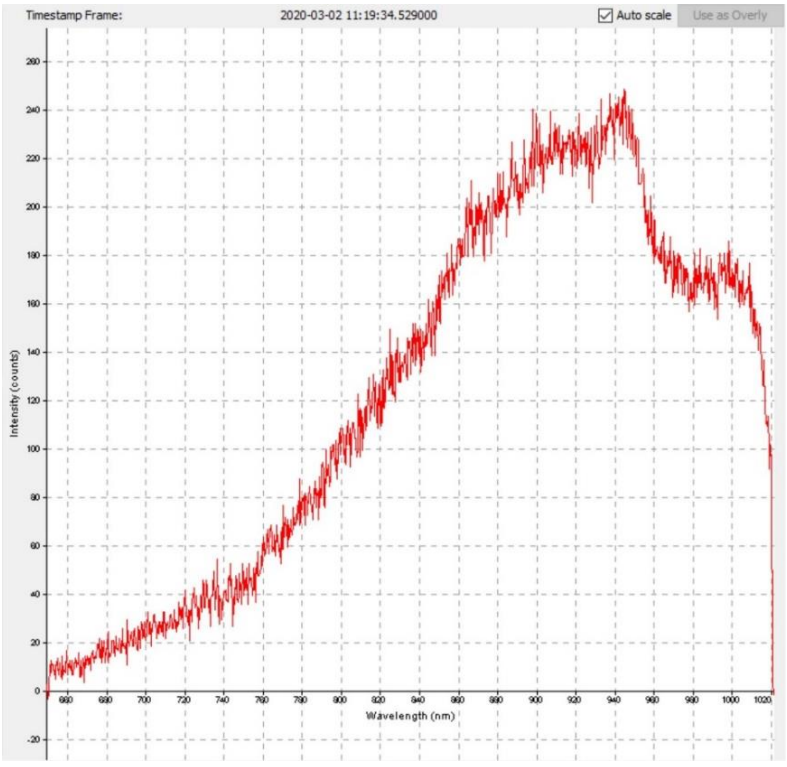

Figure 15: The real-time graphs of wavelengths vs intensities for the data collected from (a) Forehead, (b) Left back-head, (c) Right back-head

5. CONCLUSION

The quality of the fNIRS data collected can be influenced by various parameters of the experimental setup and different anatomical locations of the head where the data is collected from. Hence it is necessary to establish quantifiable standards for quality for the fNIRS data collection to compare and analyze the influence of the parameters. Our analysis shows that the quality of the fNIRS data quantified by SCI and PP , over a range of pair of wavelengths, that are influenced by various parameters such as 1) Source-detector distance 2) Integration time 3) Anatomical locations of the head.

Keeping other parameters constant, for short separation distances, though 7 mm has all the signals having high SCI, 13 mm distance has wavelength pairs showing PP of the signals higher than that of 7 mm. And for long-distance channels, 32 mm has wavelength pairs having SCI higher than 22 mm distance, but 22 mm has wavelength pairs in the center that has PP higher than that of 32 mm. Also, our analysis shows that increases the SCI and PP of 32 mm can be increased by increasing the group size of wavelengths .

The second parameter analysis shows that 100 ms of integration time is optimal for obtaining the best SCI and the PP of the signal. It would be best if the sampling frequency is between 5 Hz to 10 Hz. More research should be done in the future by analyzing the data collected between 5 Hz to 10 Hz.

Finally, the best anatomical position to get a better signal quality is found to be the forehead. But the fNIRS experiments would require studying any part of the head. Hence, through our analysis it is found that increasing the group size of wavelengths to 30, increases the SCI and PP for the signals collected from the temporal regions of the head and the wavelengths in the range 880 nm to 950 nm can be used to get optimum signals during the data collection.

REFERENCES

1. Bakker, M., Verstappen, C. C. P., Bloem, B. R., & Toni, I. (2007). Recent advances in functional neuroimaging of gait. In *Journal of Neural Transmission* (Vol. 114, pp. 1323–1331). https://doi.org/10.1007/s00702-007-0783-8
2. Huppert, T., Schmidt, B., Beluk, N., Furman, J., & Sparto, P. (2013). Measurement of brain activation during an upright stepping reaction task using functional near-infrared spectroscopy. *Human Brain Mapping*, *34*(11), 2817–2828. https://doi.org/10.1002/hbm.22106
3. Jobsis, F. (1977). Noninvasive, infrared monitoring of cerebral and myocardial oxygen sufficiency and circulatory parameters. *Science*, *198*(4323), 1264–1267. https://doi.org/10.1126/science.929199
4. Wilcox, T., & Biondi, M. (2015, May 1). fNIRS in the developmental sciences. *Wiley Interdisciplinary Reviews: Cognitive Science*. Wiley-Blackwell. https://doi.org/10.1002/wcs.1343
5. Steinbrink, J., Villringer, A., Kempf, F., Haux, D., Boden, S., & Obrig, H. (2006, May). Illuminating the BOLD signal: combined fMRI-fNIRS studies. *Magnetic Resonance Imaging*. https://doi.org/10.1016/j.mri.2005.12.034
6. Scarapicchia, V., Brown, C., Mayo, C., & Gawryluk, J. R. (2017, August 18). Functional magnetic resonance imaging and functional near-infrared spectroscopy: Insights from combined recording studies. *Frontiers in Human Neuroscience*. Frontiers Media S. A. https://doi.org/10.3389/fnhum.2017.00419
7. van de Rijt, L., van Wanrooij, M. M., Snik, A., Mylanus, E., van Opstal, A. J., & Roye, A. (2018). Measuring Cortical Activity During Auditory Processing with Functional Near-Infrared Spectroscopy. Journal of hearing science, 8(4), 9–18. https://doi.org/10.17430/1003278
8. Cope, M., Delpy, D. T., Reynolds, E. O., Wray, S., Wyatt, J., & van der Zee, P. (1988). Methods of quantitating cerebral near infrared spectroscopy data. *Advances in Experimental Medicine and Biology*, *222*, 183–189.

9. Scholkmann, F., Kleiser, S., Metz, A. J., Zimmermann, R., Mata Pavia, J., Wolf, U., & Wolf, M. (2014, January 15). A review on continuous wave functional near-infrared spectroscopy and imaging instrumentation and methodology. *NeuroImage*. https://doi.org/10.1016/j.neuroimage.2013.05.004

10. Kocsis, L., Herman, P., & Eke, A. (2006). The modified Beer-Lambert law revisited. *Physics in Medicine and Biology*, *51*(5). https://doi.org/10.1088/0031-9155/51/5/N02

11. Boas, D. A., & Dale, A. M. (2005). Simulation study of magnetic resonance imaging-guided cortically constrained diffuse optical tomography of human brain function. In *Applied Optics* (Vol. 44, pp. 1957–1968). OSA - The Optical Society. https://doi.org/10.1364/AO.44.001957

12. Pinti, P., Scholkmann, F., Hamilton, A., Burgess, P., & Tachtsidis, I. (2019). Current Status and Issues Regarding Pre-processing of fNIRS Neuroimaging Data: An Investigation of Diverse Signal Filtering Methods Within a General Linear Model Framework. *Frontiers in Human Neuroscience*, *12*. https://doi.org/10.3389/fnhum.2018.00505

13. Starck, T., Remes, J., Nikkinen, J., Tervonen, O., & Kiviniemi, V. (2010). Correction of low-frequency physiological noise from the resting state BOLD fMRI-Effect on ICA default mode analysis at 1.5 T. *Journal of Neuroscience Methods*, *186*(2), 179–185. https://doi.org/10.1016/j.jneumeth.2009.11.015

14. Yücel, M. A., Selb, J., Aasted, C. M., Lin, P.-Y., Borsook, D., Becerra, L., & Boas, D. A. (2016). Mayer waves reduce the accuracy of estimated hemodynamic response functions in functional near-infrared spectroscopy. *Biomedical Optics Express*, *7*(8), 3078. https://doi.org/10.1364/boe.7.003078

15. Fernandez Rojas, R., Huang, X., Hernandez-Juarez, J., & Ou, K. L. (2017). Physiological fluctuations show frequency-specific networks in fNIRS signals during resting state. In *Proceedings of the Annual International Conference of the IEEE Engineering in Medicine and Biology Society, EMBS* (pp. 2550–2553). Institute of Electrical and Electronics Engineers Inc. https://doi.org/10.1109/EMBC.2017.8037377

16. Brigadoi, S., Ceccherini, L., Cutini, S., Scarpa, F., Scatturin, P., Selb, J., … Cooper, R. J. (2014). Motion artifacts in functional near-infrared spectroscopy: A comparison of motion correction techniques applied to real cognitive data. *NeuroImage*, *85*, 181–191. https://doi.org/10.1016/j.neuroimage.2013.04.082

17. Yücel, M. A., Selb, J., Boas, D. A., Cash, S. S., & Cooper, R. J. (2014). Reducing motion artifacts for long-term clinical NIRS monitoring using collodion-fixed prism-based optical fibers. *NeuroImage*, *85*, 192–201. https://doi.org/10.1016/j.neuroimage.2013.06.054

18. Piaggi, P., Menicucci, D., Gentili, C., Handjaras, G., Gemignani, A., & Landi, A. (2014). Singular spectrum analysis and adaptive filtering enhance the functional connectivity analysis of resting state fMRI data. *International Journal of Neural Systems*, *24*(3). https://doi.org/10.1142/S0129065714500105

19. Pollonini, L., Olds, C., Abaya, H., Bortfeld, H., Beauchamp, M. S., & Oghalai, J. S. (2014). Auditory cortex activation to natural speech and simulated cochlear implant speech measured with functional near-infrared spectroscopy. *Hearing Research*, *309*, 84–93. https://doi.org/10.1016/j.heares.2013.11.007

20. Pollonini, L., Bortfeld, H., & Oghalai, J. S. (2016). PHOEBE: a method for real time mapping of optodes-scalp coupling in functional near-infrared spectroscopy. *Biomedical Optics Express*, *7*(12), 5104. https://doi.org/10.1364/boe.7.005104

21. Gagnon, L., Perdue, K., Greve, D. N., Goldenholz, D., Kaskhedikar, G., & Boas, D. A. (2011). Improved recovery of the hemodynamic response in diffuse optical imaging using short optode separations and state-space modeling. *NeuroImage*, *56*(3), 1362–1371. https://doi.org/10.1016/j.neuroimage.2011.03.00

22. Brigadoi, S., & Cooper, R. J. (2015). How short is short? Optimum source–detector distance for short-separation channels in functional near-infrared spectroscopy. *Neurophotonics*, *2*(2), 025005. https://doi.org/10.1117/1.nph.2.2.025005

23. Saager, R., & Berger, A. (2008). Measurement of layer-like hemodynamic trends in scalp and cortex: implications for physiological baseline suppression in functional near-infrared spectroscopy. *Journal of Biomedical Optics*, *13*(3), 034017. https://doi.org/10.1117/1.2940587

24. Gregg. (2010). Brain specificity of diffuse optical imaging: improvements from superficial signal regression and tomography. *Frontiers in Neuroenergetics*. https://doi.org/10.3389/fnene.2010.00014

25. Scarpa, F., Brigadoi, S., Cutini, S., Scatturin, P., Zorzi, M., Dell'Acqua, R., & Sparacino, G. (2013). A reference-channel based methodology to improve estimation of event-related hemodynamic response from fNIRS measurements. *NeuroImage*, *72*, 106–119. https://doi.org/10.1016/j.neuroimage.2013.01.02

26. Goodwin, J. R., Gaudet, C. R., & Berger, A. J. (2014). Short-channel functional near-infrared spectroscopy regressions improve when source-detector separation is reduced. *Neurophotonics*, *1*(1), 015002. https://doi.org/10.1117/1.nph.1.1.015002

27. Pinti, P., Scholkmann, F., Hamilton, A., Burgess, P., & Tachtsidis, I. (2019). Current Status and Issues Regarding Pre-processing of fNIRS Neuroimaging Data: An Investigation of Diverse Signal Filtering Methods Within a General Linear Model Framework. *Frontiers in Human Neuroscience*, *12*. https://doi.org/10.3389/fnhum.2018.00505